University of Cyprus
Department of Physics

Optical spectroscopy of heterojunctions of $CsPbBr_3$ Perovskite nanocrystals and Blatter Radicals

Author: Rafael Agathangelou

Supervisor:
Assoc. Prof. Grigorios Itskos

Academic Year: 2024 - 2025

A thesis submitted in partial fulfillment of the requirements for the Bachelor of Science degree in Physics, in the Department of Physics of the University of Cyprus.

“There’s plenty of room at the bottom.”

— Richard Feynman

Acknowledgments

I would like to express my deepest gratitude to my supervisor, Dr. Grigorios Itskos, for his exceptional guidance, support, and insight throughout this journey. His expertise and mentorship have been instrumental in shaping my scientific thinking and approach, and I am sincerely thankful for the opportunities he has provided me. I am also grateful to Dr. Paris Papagiorgis and Andreas Manoli, as well as the rest of the team, for their invaluable assistance in the laboratory and their support throughout the data analysis process. Their knowledge, patience, and willingness to share their experience have been crucial to the completion of this work and my growth as a researcher.

Special thanks to the Kovalenko group at ETH Zurich and the Koutentis group from the Department of Chemistry for providing the materials used in this study. This work could not have been carried out without their cooperation and the recourses they generously provided.

Lastly, I would like to thank my friends, who have been a constant source of support, encouragement, and much needed distraction. Whether it was late night brainstorming sessions, moral support during deadlines, or simply making sure I remembered to eat and laugh, their presence has been essential, not just during this thesis, but throughout my entire degree. I am especially grateful to one friend in particular, whose unwavering support made more of a difference than she may ever realize.

Motivation

Semiconductor nanocrystals, particularly lead halide perovskites (LHPs) like $CsPbBr_3$, have garnered considerable interest due to their exceptional optoelectronic properties, such as high photoluminescence quantum yields, tunable emission wavelengths, and remarkable defect tolerance. These properties make them highly suitable as classical and quantum emitters, with applications ranging from quantum dot light-emitting diodes (QLEDs) for high-performance displays and televisions, to single photon sources and detectors. Moreover, LHP nanocrystals are emerging as promising materials for advanced applications such as photocatalysis, solar cells, and spintronics, leveraging their efficient light absorption, charge carrier dynamics, tunable electronic states and high spin-orbit coupling and optically addressable spin states.

A relatively unexplored class of materials are the heterojunctions formed between LHP nanocrystals and organic radical molecules. These systems exhibit electron/hole donor-acceptor behavior similar to that of closed-shell organic compounds, while also offering intriguing magnetic properties due to the presence of unpaired electrons in the radical species. Blatter radicals specifically, have attracted attention due to their robust chemical stability, intrinsic magnetic properties, and unique electronic characteristics originating from their stable unpaired electron spins. The exceptional stability of Blatter radicals compared to conventional radicals makes them practically viable candidates for applications in molecular spintronics, magnetic resonance imaging, and as active components in sensors and novel organic electronic devices.

Motivated by the aforementioned properties of perovskite NCs and Blatter radicals and the shortage of relevant studies combining the two material families, this thesis investigates the photophysics of heterojunctions formed between $CsPbBr_3$ nanocrystals and the parent blatter radical, formally known as 1-phenyl-3-phenylaminopyrazol-2-yl. The goal of this study is to implement spectroscopic methods, such as steady-state and time resolved photoluminescence, as well as transient absorption spectroscopy in combination with EPR measurements to probe the presence of charge and spin transfer pathways mediated by the NC-radical interface. In addition to photoinduced charge transfer processes, such measurements could also give insight into several other aspects of this hybrid system, such as native ligand displacement and passivation of the nanocrystal's surface from the radicals, and possible exciton-unpaired spin interactions.

In the long term, the desired functionality would be to use the unpaired radical spin to fine tune electronic properties of the NCs such as exciton lifetimes, spin polarization, and charge carrier dynamics. Such functionality would be of interest to fields that include spintronics, photocatalysis, and quantum information systems, underscoring the broad technological applicability of such systems.

Contents

List of Abbreviations

NC(s) - Nanocrystal(s)

MHP(s) - Metal-Halide Perovskite(s)

LHP(s) - Lead-Halide Perovskite(s)

QY - Quantum yield

CT - Charge transfer

FRET - Förster resonance energy transfer

HOMO - Highest occupied molecular orbital

SOMO - Singly occupied molecular orbital

LUMO - Lowest unoccupied molecular orbital

SC - Spin-coated

PL - Photoluminescence

PLE - Excitation photoluminescence

TCSPC - Time-correlated single photon counting

TRPL - Time-resolved photoluminescence

VB/CB - Valence band/Conduction band

Chapter 1

Nanocrystals

1.1 Quantum confinement in semiconductors

As transistors continue to shrink in modern electronic and optoelectronic devices, the need to understand size-dependent effects is becoming increasingly significant. The primary motivation for studying nano-scale semiconductor crystallites, nanocrystals for short, is understanding what happens when a material becomes very small. Intuitively, the optical and electronic properties of solids wouldn't depend on the size of the crystal, but this is only true if the size is relatively large. As we restrict the motion of carriers in a semiconductor, what is known as quantum confinement, unique effects arise due to the changes in carrier dynamics. By employing the basic principles of quantum mechanics, we are able to quantitatively describe these effects arising from this apparent size dependency.

1.1.1 Size effects

Heisenberg's uncertainty principle states that there is a limit to how precisely we can simultaneously measure a particle's position and momentum. Mathematically, it is given by inequality 1.1.

$$\Delta x \Delta p_x \geq \frac{\hbar}{2} \tag{1.1}$$

where $\Delta x,\ \Delta p_x$ are the uncertainties in position and momentum respectively. If a particle of mass m is otherwise free to move in the x-direction, the uncertainty in momentum arising from this principle gives the particle an additional kinetic energy E_{conf}.

$$E_{conf} = \frac{\Delta p_x^2}{2m} \sim \frac{\hbar^2}{8m\Delta x^2} \tag{1.2}$$

If this energy arising from confinement is comparable to the kinetic energy due to thermal motion in the x-direction, then it becomes significant. Using eq. 1.2, one can show that :

$$E_{conf} \sim \frac{\hbar^2}{8m\Delta x^2} \gtrsim \frac{1}{2} k_B T$$

$$\Rightarrow \Delta x \lesssim \frac{\hbar}{2}\sqrt{\frac{1}{mk_BT}} \tag{1.3}$$

This expression gives us an idea of how small a system must be, in order for quantum confinement effects to arise[1], and is equivalent to saying that Δx must be comparable to or smaller than the de Broglie wavelength for the thermal motion. As seen in Fig. 1.1, the stronger the confinement, the better the energy state discretization.

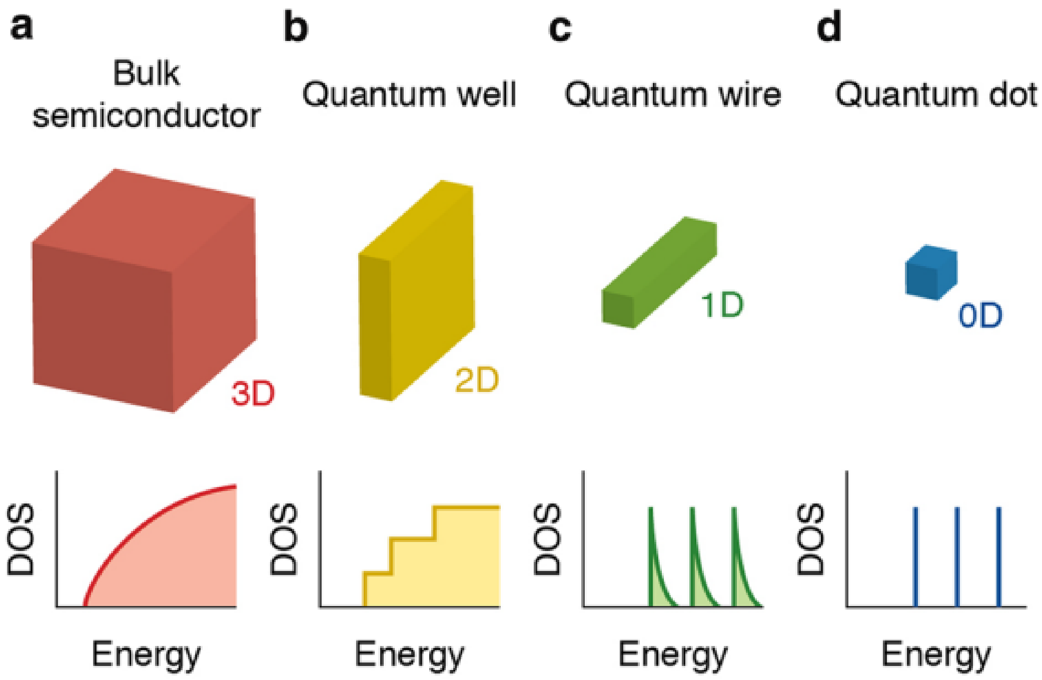

Fig. 1.1 Illustration of the energy level structure in **(a)** Bulk crystals and **(b-d)** structures with reduced dimensionality. In a quantum well **(b)**, carrier movement is confined in one dimension, in a quantum wire **(c)** in two dimensions and in a quantum dot **(d)** in all three dimensions. Taken from Freddy Rabouw and Celso Donega [22].

As carriers are confined to a smaller and smaller volume, the electrostatic (Coulomb) interactions between the thermally or photo excited electron-hole pairs, also known as excitons, serve to modify the properties of nanoscale crystallites compared to bulk, by introducing effects such as:

- **Altered carrier/exciton dynamics** : Since the electron and hole wavefunctions can have a larger overlap, recombination rates and thus radiative lifetimes differ significantly from bulk crystals.

- **Reduced or discretized density of states (DOS)** : As dimensionality is reduced, the number of available states is decreased, becoming discrete in the limit of the strong confinement regime, modifying how carriers and excitons are distributed.

- **Surface reactivity** : The surface to volume ratio increases, meaning a higher fraction of atoms is on the surface, with an increased contribution from surface states, if they lie energetically close to the energy gap.

---

[1] For example, at room temperature a typical semiconductor such as Silicon with an electron effective mass of $m_e^* = 0.01m_e$ can exhibit quantum effects due to confinement at sizes around 10nm.

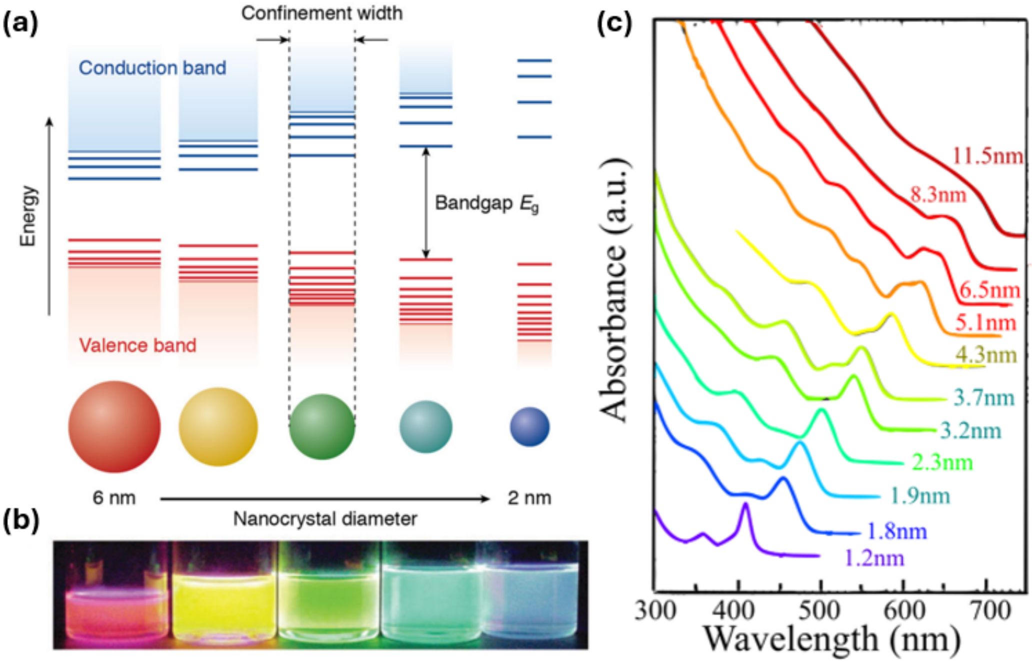

Fig. 1.2 Schematic representation of the effects of **(a)**confinement on the bandgap of CdSe NCs , **(b)** the emitted light when exposed to a UV light source, and **(c)** the absorption spectra at different NC sizes. Adapted from Freddy Rabouw and Celso Donega [22] **(a-b)** and Alexander L. Efros and Louis E. Brus [8] **(c)**.

All these effects can be utilized for fine-tuning of the optoelectronic properties of our material, as seen in Fig. 1.2, where enhanced and size-dependent light absorption is observed, as well as tailoring of the bandgap through the whole visible spectrum. It's therefore clear that nanocrystals offer outstanding optical properties and unparalleled control over material properties, making them highly promising for next-generation optoelectronic, energy, biomedical, and nanotechnology applications.

One of the most mature and commercially successful implementations is in quantum dot light emitting diodes (Q-LEDs), where nanocrystals serve as tunable, high-efficiency emitters in next-generation display technologies. Their narrow and size-tunable emission spectra allow for enhanced color purity and brightness in televisions and monitors, outperforming conventional phosphor-based systems. Similarly, quantum dots are used in photodetectors and single-photon sources, where their discrete energy levels and controllable recombination lifetimes enable precise photon emission, essential for quantum optics and information systems.

Other applications under investigation, are in the field of photovoltaics, where nanocrystals offer unique advantages such as multi-exciton generation and hot-carrier extraction, which could surpass the Shockley-Queisser efficiency limit in traditional solar cells. Their large surface-to-volume ratio also makes them ideal for photocatalytic applications, where surface interactions with reactants can be harnessed for chemical transformations under light exposure. Furthermore, due to their spin-sensitive excitonic properties and the ability to be integrated with magnetic or spin-active materials, quantum dots are increasingly explored in the field of spintronics, with the goal of developing light-controlled spin filters or qubits for quantum computing architectures.

1.1.2 Electronic structure

In a bulk crystal, the large spatial extent of the electron and hole wavefunctions, along with periodic boundary conditions, leads to the formation of bands with almost continuous energy distributions. By contrast, reducing the crystal dimensions to a few nanometers imposes boundary conditions that sharply quantize the energy levels, such that the carriers can only occupy specific, discrete energies.

A simple model that can provide a quantitative description of this size-dependence is the particle in a sphere model. In general, this model considers an arbitrary particle of mass m in a spherical potential well $V(r)$ of radius a.

$$V(r) = \begin{cases} 0 \ , & r < a \\ \infty \ , & r > a \end{cases} \tag{1.4}$$

According to Griffiths (ref. [11]), the solutions to the Schrödinger equation for such a potential are :

$$\Phi_{n,\ell,m}(r,\theta,\phi) = C\frac{j_\ell(k_{n,\ell}r)\, Y_\ell^m(\theta,\phi)}{r} \tag{1.5}$$

where C is a normalization constant, $Y_\ell^m(\theta,\phi)$ is a spherical harmonic, $j_\ell(k_{n,\ell}r)$ is the ℓth order spherical Bessel function, and

$$k_{n,\ell} = \frac{\alpha_{n,\ell}}{a}$$

with $\alpha_{n,\ell}$ being the nth root of j_ℓ. The energy of the particle is given by :

$$E_{n,\ell} = \frac{\hbar^2 k_{n,\ell}^2}{2m_o} = \frac{\hbar^2 \alpha_{n,\ell}^2}{2m_o a^2}$$

Considering the symmetry of the problem, the eigenfunctions 1.5 are simple atomic-like orbitals that can be labeled by the quantum numbers n (1, 2, 3...), ℓ (s, p, d...), and m. It should also be noted that the energy of the particle is inversely proportional to the square of the well's radius, meaning there is a strong dependency on the size of the system.

This single-well model may not seem useful in the case of real solids with a periodic crystal lattice, meaning a series of such potential wells. However, through a series of approximations and use of Bloch's theorem (eq. 1.6), the electrons and holes may be treated as particles of effective mass m_e^* and m_h^* respectively, inside a sphere of constant potential. According to Bloch's theorem, in the effective mass approximation, the electronic wavefunctions can be written as :

$$\Psi_{n\mathbf{k}}(\vec{r}) = u_{n\mathbf{k}}(\vec{r})\exp(i\vec{k}\cdot\vec{r}) \tag{1.6}$$

where $u_{n\mathbf{k}}$ is a function with the periodicity of the crystal lattice and the wavefunctions are labeled by the band index n and wavevector k. For a single particle, the wavefunction can be written as a linear combination of these Bloch functions.

$$\Psi_{sp}(\vec{r}) = \sum_{\vec{k}} C_{n\vec{k}}\ u_{n\vec{k}}(\vec{r})\ \exp(i\vec{k}\cdot\vec{r}) \tag{1.7}$$

where $C_{n\vec{k}}$ are expansion coefficients, which ensure that the sum satisfies the spherical boundary condition of the nanocrystal. Assuming that the functions $u_{n\vec{k}}$ have a weak $\vec{k}$ dependence, then we can write :

$$\Psi_{sp}(\vec{r}) = u_{n0}(\vec{r}) \sum_{\vec{k}} C_{n\vec{k}} \exp(i\vec{k}\cdot\vec{r}) = u_{n0}(\vec{r}) f_{sp}(\vec{r}) \tag{1.8}$$

where $f_{sp}(\vec{r})$ is the single particle envelope function. Since the periodic functions u_{n0} can be determined within the tight-binding approximation as a sum of atomic wavefunctions, φ_n,

$$u_{n0}(\vec{r}) \approx \sum_{i} C_{ni}\ \varphi_n(\vec{r}-\vec{r}_i) \tag{1.9}$$

For spherically shaped nanocrystals with a potential barrier that can be approximated as infinitely high, the envelope functions of the carriers are given by the particlein-a-sphere solutions derived earlier (eq. 1.5). Therefore, the wavefunctions of the carriers inside the nanocrystal can be written as :

$$\Psi_e(\vec{r_e}) = C_e u_e \left(\frac{j_{L_e}\left(k_{n_e,L_e} r_e\right) Y_{L_e}^{m_e}}{r_e}\right) \tag{1.10}$$

$$\Psi_h(\vec{r_h}) = C_h u_h \left(\frac{j_{L_h}\left(k_{n_h,L_h} r_h\right) Y_{L_h}^{m_h}}{r_h}\right) \tag{1.11}$$

where u_e, u_c depend on the exact structure and composition of the material's unit cell. Using these in the strong confinement regime of NCs, we can now write down the wavefunction for the exciton (electron-hole pair) states in the nanocrystal as :

$$\Psi_{exc}(\vec{r_e},\vec{r_h}) = \Psi_e(\vec{r_e})\Psi_h(\vec{r_h}) = C\left[u_e\left(\frac{j_{L_e}\left(k_{n_e,L_e} r_e\right) Y_{L_e}^{m_e}}{r_e}\right)\right]\left[u_h\left(\frac{j_{L_h}\left(k_{n_h,L_h} r_h\right) Y_{L_h}^{m_h}}{r_h}\right)\right] \tag{1.12}$$

with energies[2] :

$$E_{exc}\left(n_h L_h n_e L_e\right) = E_g + \frac{\hbar^2}{2a^2}\left\{\frac{\alpha_{n_h,L_h}^2}{m_h^*} + \frac{\alpha_{n_e,L_e}^2}{m_e^*}\right\} - E_c \tag{1.13}$$

Therefore, in the effective mass approximation, each of the electron and hole levels depicted can be described by an atomic-like orbital that is confined within the nanocrystal (1S, 1P, 1D, 2S, etc.). The main difference between nanocrystals and bulk crystals is this increased localization of the energy states, as seen in Fig. 1.3c[3] , caused by the confinement of carriers.

---

[2] Here, the term E_C is the first-order Coulomb correction, i.e the exciton binding energy, accounting for the interaction between carriers. Its exact value depends on the confinement regime and is therefore not expanded upon, as we are simply examining a generalized case. More details regarding the theoretical framework can be found in Ashcroft (ref. [2]) and Klimov (ref. [14]).

[3] Here, the continuous lines forming the two rectangles represent the continuous energy band observed in bulk CdSe, while the discrete horizontal lines represent the energy levels in a CdSe NC.

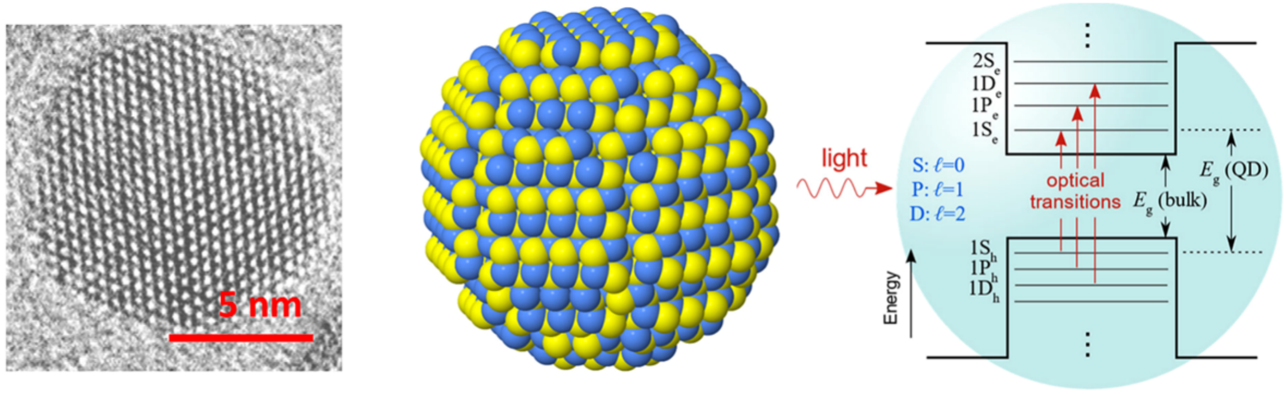

(a) (b) (c)

Fig. 1.3 Illustration of **(a)** a TEM image of a CdSe NC, **(b)** a model of the atomic structure of the NC, and **(c)** the electron and hole states within the NC. Adapted from Alexander L. Efros and Louis E. Brus [8].

1.1.2.1 Excitons

When a photon with sufficient energy is absorbed by a semiconductor, it typically promotes an electron from the valence band to the conduction band, leaving behind a positively charged hole. Due to their opposite charges, the electron and hole can form a bound state via Coulomb attraction, analogous to a hydrogen atom[4]. This quasiparticle is known as an exciton. Excitons are electrically neutral and can migrate through the material, making them crucial to understanding light-matter interactions in nanocrystals and quantum dots.

There are two primary classes of excitons, shown in Fig. 1.4, namely Wannier-Mott, or free, excitons which are typically found in semiconductors, and Frenkel, or strongly bound, excitons common in molecular crystals and insulators. The former are characterized by their large spatial extent, often spanning multiple unit cells, and their relatively low binding energy (on the order of meV), making them observable primarily at low temperatures. In contrast, Frenkel excitons are tightly bound, with radii comparable to the size of a unit cell and binding energies up to 1 eV, making them stable even at room temperature.

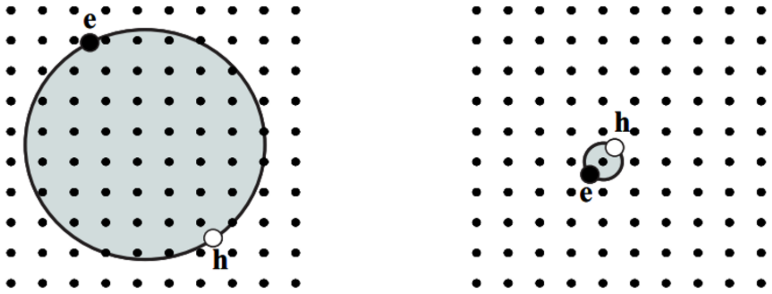

(a) (b)

Fig. 1.4 Illustration of **(a)** a free, Wannier-Mott, exciton, and **(b)** a tightly bound, Frenkel, exciton. Adapted from Fox M. [10].

---

[4] Hence the hydrogen atom-like nature of the exciton's wavefunction (eq. 1.12) derived previously in section 1.1.2. The specific energies required for the formation of excitons is given by eq. 1.13.

In bulk semiconductors, excitonic effects are subtle and often suppressed by doping or thermal fluctuations. Cooling the bulk crystal, can reveal these suppressed effects in the crystal's absorption spectrum, as seen in Fig. 1.5a. However, in nanocrystals, where carriers are confined in all spatial dimensions, the overlap between electron and hole wavefunctions is significantly enhanced, even at room temperature, as shown in Fig. 1.5b. This confinement increases the binding energy of excitons, alters radiative recombination rates, and leads to discrete excitonic absorption features below the bandgap. These features play a dominant role in determining the optical properties of quantum dots.

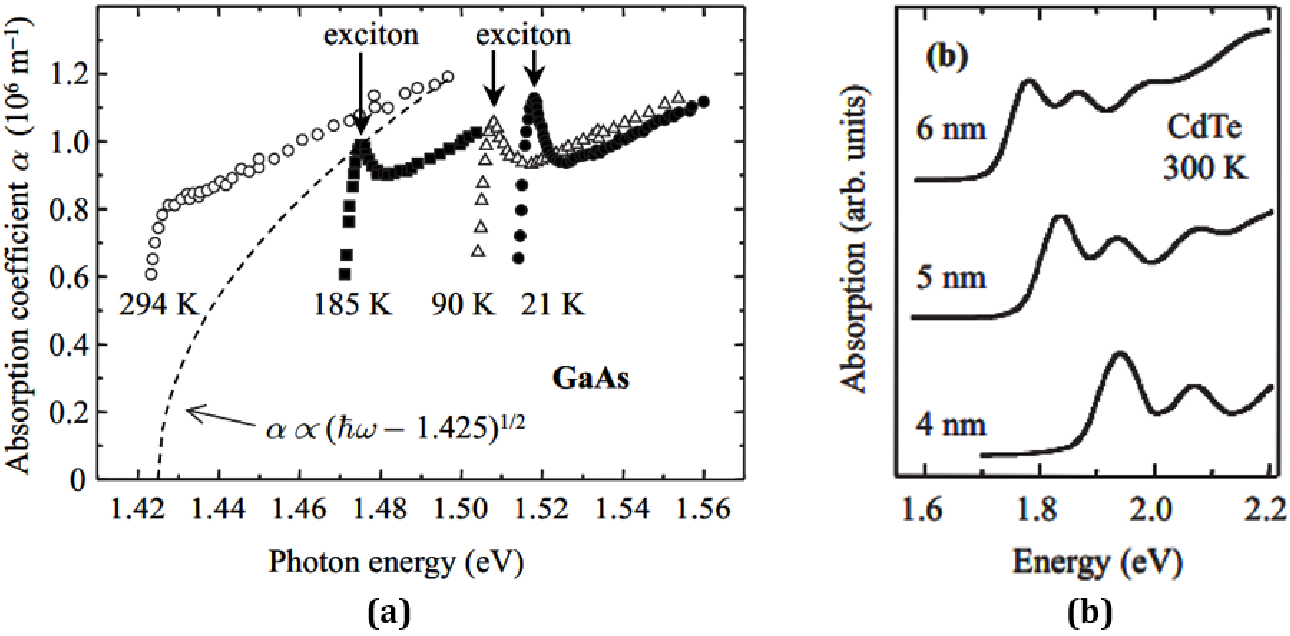

Fig. 1.5 Excitonic absorption of **(a)** bulk GaAs between 21 K and 294 K, and **(b)** of CdTe colloidal quantum dots in solution form at room temperature. The dashed line in **(a)** is an attempt to fit the absorption edge to extract a bandgap energy equal to 1.425 eV, which is appropriate for GaAs at 294 K. Adapted from Fox M. [10].

Evidently, excitonic features dominate the optical spectra in nanocrystals due to strong quantum confinement, which leads to discrete energy levels and enhanced Coulomb interactions. The resulting exciton binding energies can be an order of magnitude larger than in the bulk, allowing excitons to remain stable at room temperature. This stability is key for high-efficiency light emission, making excitonic transitions directly observable in photoluminescence and absorption measurements. Moreover, the fine structure of excitonic states significantly influences recombination dynamics and quantum coherence, properties that are essential in designing quantum light sources, lasers, and exciton-based qubits.

1.1.3 Carrier and Exciton relaxation

Carrier and exciton generation in semiconductor NCs can occur through many different processes such as thermal excitation, impact ionization or electrical injection, but the most common processes is optical excitation. This is possible through the photoelectric effect, where an electron in the valance band (VB) absorbs a photon, with energy greater than or equal to the NC's bandgap, and transitions to a higher energy in the conduction band (CB). However, these carriers typically relax quickly toward lower energy states, by interacting with phonons[5], eventually reaching the conduction and valence band edges, and recombining after a characteristic time τ, also known as carrier lifetime. This characteristic time is defined by the total transition rate of the system.

$$\tau = \frac{1}{W_{tot}} = \frac{1}{W_R + W_{NR}} \tag{1.14}$$

where W_R, W_{NR} are the radiative and non-radiative carrier recombination rates. These involve several interconnected physical processes occurring on distinct timescales, which directly influence the optical properties and the performance of optoelectronic devices utilizing these materials. A similar process is valid for Coulombically bound electron-hole paris in the forms of excitons. Thus, understanding carrier and exciton relaxation mechanisms is critical to understanding and optimizing the photonic performance of NC-based devices.

1.1.3.1 Radiative transitions

The probability for an electron to make an optical transition from the valence band, call it the ground state $|0\rangle$, to the conduction band, the exciton state $|\Psi_{ehp}\rangle$, by absorbing a photon with a polarization vector $\vec{e}$, is given by the dipole matrix element :

$$P = |\langle \Psi_{ehp} | \vec{e} \cdot \hat{p} | 0 \rangle|^2 \tag{1.15}$$

where $\hat{p}$ is the momentum operator. In the strong confinement regime of NCs, where carriers can be treated independently[6], this matrix element can be written in terms of the single particle states as seen on the left side of Eq. 1.16. Since the envelope functions $f_e,\ f_h$ are slowly varying in terms of $\vec{r}$ relative to the Bloch functions $u_e,\ u_h$, so we can separate the two.

$$P = |\langle \Psi_e | \vec{e} \cdot \hat{p} | \Psi_h \rangle|^2 = |\langle u_c | \vec{e} \cdot \hat{p} | u_v \rangle|^2 \, |\langle f_e | f_h \rangle|^2 \tag{1.16}$$

Because of the orthonormality of the envelope functions, their product allows only specific transitions.

$$P = |\langle u_c | \vec{e} \cdot \hat{p} | u_v \rangle|^2 \, \delta_{n_e,n_h} \delta_{L_e,L_h} \tag{1.17}$$

Therefore, the selection rules for optical generation of carriers are $\Delta L = 0$ and $\Delta n = 0$. The process is similar for exciton recombination by photon emission, namely transitions from the exciton state, to the ground state.

$$P = |\langle 0 | \vec{e} \cdot \hat{p} | \Psi_{ehp} \rangle|^2 = |\langle \Psi_h | \vec{e} \cdot \hat{p} | \Psi_e \rangle|^2 \tag{1.18}$$

It should be noted that these probabilities regard photons of specified polarization $\vec{e}$, coming

---

[5] Quantized crystal lattice vibrations.

[6] This largely due to the confinement energy discussed in section 1.1.1. As the confinement increases, so does the kinetic energy of the carriers, up to the point where it dominates over the Coulombic interaction between the carriers, allowing us to treat them independently.

in from some arbitrary direction $\hat{k}$. The total probability of carrier generation/recombination would be given by the sum of all possible incident light polarizations for every possible propagation vector.

$$P^{tot}_{i\to j} = \int d\Omega \sum_{\lambda=1}^{2} \left| \langle \Psi_\mathrm{j} \,|\, \vec{e}_\lambda(\hat{k}) \cdot \hat{p} \,|\, \Psi_\mathrm{i} \rangle \right|^2 . \tag{1.19}$$

where λ represents the two possible polarizations for any propagation vector $\vec{k}$ and $d\Omega(\hat{k})$ is the infinitesimal solid angle. These processes have characteristic times anywhere from hundreds of picoseconds to hundreds of nanoseconds, largely depending on the carrier dynamics and available decay pathways [5].

1.1.3.2 Non-radiative transitions

In addition to radiative processes driven by dipole allowed transitions, excited carriers in nanocrystals can also relax without emitting photons through non-radiative pathways. Such processes often dominate under conditions where phonon coupling, defect states, or Auger-type carrier-carrier interactions are strong, causing the excited electron-hole pair to lose energy via internal mechanisms rather than photon emission.

A general non-radiative transition rate can be described via Fermi's Golden Rule, analogously to radiative processes, but with a different interaction Hamiltonian $\hat{H}_\mathrm{nr}$ instead of the dipole (momentum) operator $\hat{p}$. Symbolically,

$$W_\mathrm{nr} = \frac{2\pi}{\hbar} \left| \langle \Psi_\mathrm{f} \,|\, \hat{H}_\mathrm{nr} \,|\, \Psi_\mathrm{i} \rangle \right|^2 \rho(E_\mathrm{f}), \tag{1.20}$$

where $|\Psi_\mathrm{i}\rangle$ and $|\Psi_\mathrm{f}\rangle$ are the initial and final many-body states of the electron–hole pair, and $\rho(E_\mathrm{f})$ is the density of available final states at the relevant energy E_f. The exact form of $\hat{H}_\mathrm{nr}$ depends on the primary mechanism by which the carrier relaxes. The main types of such processes are :

- **Phonon-assisted relaxation** : In the strong confinement regime of NCs, the overlap of electron/hole wavefunctions with certain phonon modes can provide a route for electrons or holes to shed excess energy. This interband relaxation is ultrafast, with typical durations in the picosecond scale.

- **Auger recombination** : A three body interaction, where the excess energy from recombination between two carriers is not released in the form of an emitted photon, but transferred to a third carrier, promoting it to a higher energy state.

- **Trap-assisted recombination** : Defect states, created by imperfections in the crystal lattice, can provide a decay pathway that bypasses the radiative recombination pathway. The energy dissipation mechanism mediating this relaxation depends on the depth of the trap state. If it lies energetically close to an edge, then photon emission is possible, but with a smaller energy, meaning the emission spectrum would be slightly red-shifted[7]. If

---

[7] Meaning a peak localized at a larger wavelength, as energy is inversely proportional to wavelength.

the trap state is deep inside the bandgap, the carrier may relax down to the VB through phonon-assisted relaxation, completely bypassing radiative recombination.

Such processes are typically ultra-fast, with durations in the picosecond regime [5]. Rough schematics of the radiative and non-radiative processes described can be seen in Fig. 1.6.

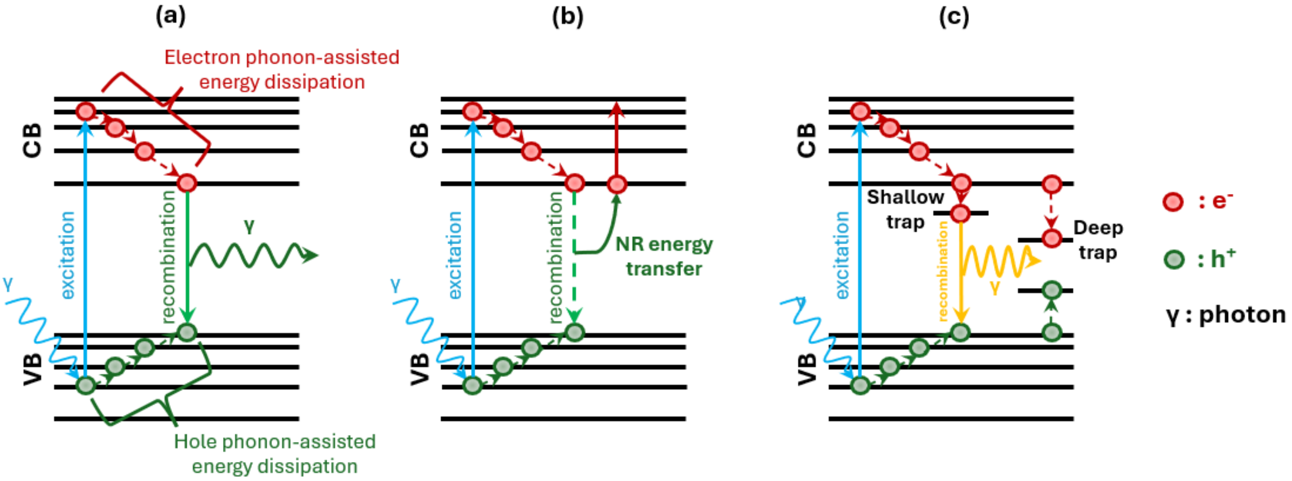

Fig. 1.6 Schematic representation of **(a)** photo-excitation, carrier relaxation and radiative recombination, **(b)** Auger recombination and **(c)** trap-assisted relaxation of carriers.

1.1.3.3 Charge transfer

When two nanostructures come into close proximity to form what is known as a heterojunction, it is possible for carriers from one structure to transfer into energetically available states in the second structure. Typically the transfer occurs after photo-excitation of one of the heterojunction materials in a process known as photoinduced charge transfer resulting in a net charge on both structures. When a single carrier relaxes in such a way, we get a net charge on both structures,. The mechanisms that drive such processes depend on the nature of the interaction between the two nanostructures. The most common of these mechanisms are :

- **Quantum tunneling** : When the carrier wavefunctions of the two structures significantly overlap, electron or hole tunneling may occur, as seen in Fig. 1.7. The magnitude of this overlap is dependent on the spatial extent of the wavefuntions, the distance between the two structures and the barrier characteristics at the interface.

- **Phonon-assisted Hopping** : In addition to carrier wavefunction overlap assisting in the transport of the carrier through the interface barrier, the energy to overcome this potential barrier may be provided by phonons, in a process known as Hopping. The CT rate for such a process is heavily dependent on the vibrational modes and temperature of the system.[26]

In general, the probability of charge transfer (CT) from an initial state $\left|\Psi_i^D\right\rangle$ of the donor (D) to the final state $\left|\Psi_f^A\right\rangle$ in the acceptor (A) can be described by Fermi's golden rule :

$$W_{CT} = \frac{2\pi}{\hbar}|\langle\Psi_f^A|\hat{H}_{int}|\Psi_i^D\rangle|^2\rho(E_f) \tag{1.21}$$

where $\hat{H}_{int}$ represents the interaction Hamiltonian, and $\rho(E_f)$ is the density of energetically available states in the acceptor. The exact form of $\hat{H}_{int}$, and thus the transition rate W_{CT}, is dependent on the dominating mechanism mediating the CT between the two structures.

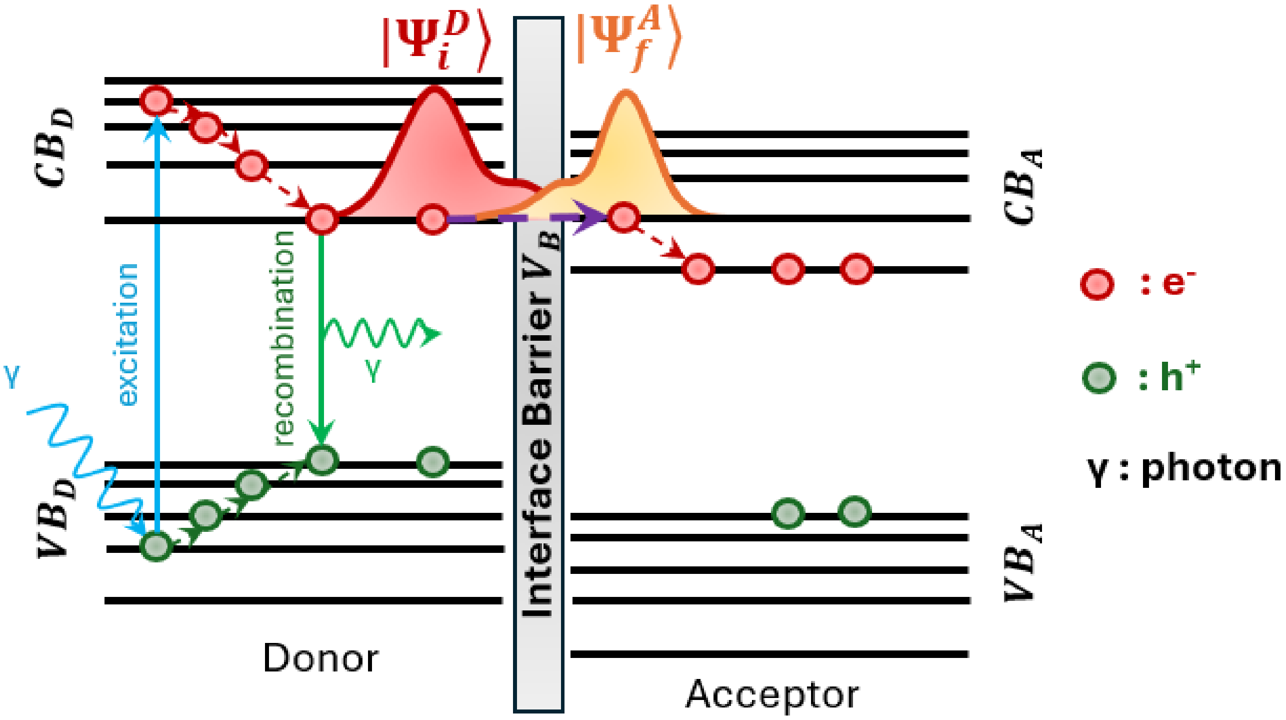

Fig. 1.7 Schematic representation of electron transfer from a donor NC to an acceptor NC, mediated by quantum tunneling.

Considering all of the above, CT efficiency and dynamics are strongly influenced by the electronic structure and vibrational properties of the donor and acceptor. Therefore, in order to study CT in NC heterojunctions, one needs to have an understanding of these properties.

1.1.3.4 Energy transfer

In addition to charge transfer, where carriers are transported between the two nanostructures, excitons formed in the donor can transfer their energy non-radiatively to the acceptor in a process known as energy transfer (ET). In contrast to CT, ET does not necessarily involve the actual transport of electrons and holes though the interface barrier, it can also rely on electromagnetic interactions, such as dipole-dipole coupling, between the donor's exciton and energetically resonant states in the acceptor.

The probability of ET from an excited donor state $|\Psi^D_{exc}\rangle$ to an acceptor state $|\Psi^A_{exc}\rangle$, is again described by Fermi's golden rule 1.21. The two main mechanisms that mediate such processes are :

- **Dexter Energy Transfer (DET)** : Similar to CT via tunneling, DET is mediated by the overlap of the donor and acceptor electron-hole pair wavefunctions and is therefore prominent at very short distances ($\sim 1nm$).

- **Förster Resonance Energy Transfer (FRET)** : Mediated by dipole-dipole interactions[8], FRET is prominent when donor emission and acceptor absorption spectra overlap significantly. However, due to the nature of the interaction, the overlap integral decreases rapidly with distance ($\sim \frac{1}{R^6}$), and therefore FRET typically occurs at distances between 1-10nm.

Due to the quantum confinement of the envelope functions in semiconductor nanocrystals, energy transfer mechanisms and efficiencies strongly depend on nanocrystal size, shape, and interface structure. Control of these parameters allows tuning of energy transfer properties for optimized optoelectronic and photonic applications.

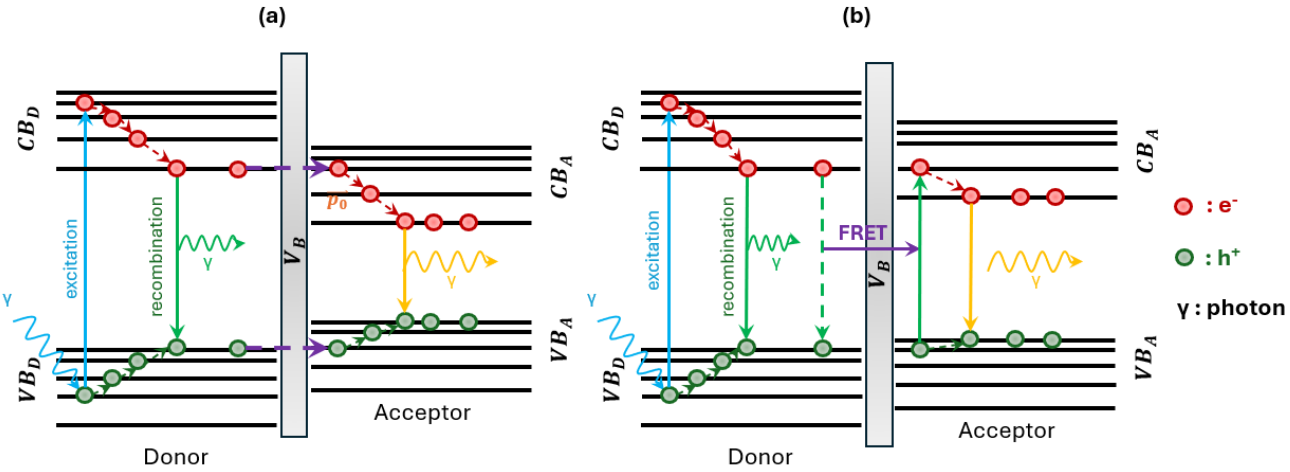

Fig. 1.8 Schematic representation of **(a)** Dexter energy transfer, and **(b)** Förster resonance energy transfer between two nanocrystals.

1.2 Metal-Halide Perovskite nanocrystals

Metal-halide perovskites (MHPs), such as $CsPbBr_3$, are semiconductor-like materials that have attracted considerable attention due to their remarkable photonic properties. Similar to conventional semiconductors (e.g., silicon, GaAs, CdSe), MHPs exhibit a direct band gap suitable for absorbing and emitting visible light, with direct transitions, strong absorption coefficients, and long carrier diffusion lengths. Their high customizability has generated a lot of interest in recent years, with research regarding their potential applications in various fields.

1.2.1 Crystal structure

In general, MHPs have a crystal structure of ABX_3, as seen in Fig. 1.9, where A and B denote two cations of different sizes and X is an anion. Essentially, the A-site cation primarily influences lattice stability and can affect phase transitions. The electronic band structure on the other hand is mainly defined by the BX_6 octahedra. Another characteristic of the soft ionic

---

[8] The dipole-dipole interaction in FRET is between the donor's exciton dipole moment and the acceptor's energetically available transition dipole moment.

crystal structure of perovskites is that halide anion exchange reactions can happen easily, resulting in control of the energy gap through the visible spectrum, as demonstrated by Kovalenko M. et al [1].

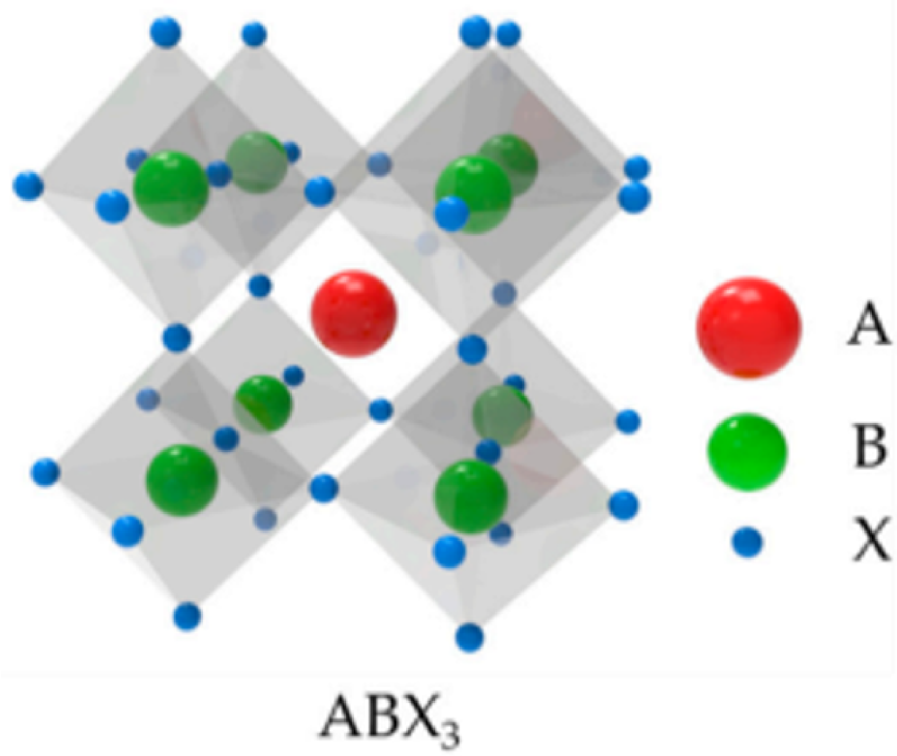

Fig. 1.9 Schematic representation of the general ABX_3 crystal structure of perovskites. Adapted from Seunghyun Rhee et al [23].

Common representatives of these cations and anions are A = Cs^+, $CH_3NH_3^+$ (MA^+), $CH(NH_2)_2^+$ (FA^+), $CH_3CH_2NH_3^+$, B = Pb^{2+}, Sn^{2+}, Cu^{2+}, and X = Cl^-, Br^-, and I^- (halogens). In LHP NCs specifically, the B-site cation is Lead (Pb^{2+}), and for the A-site cation Cesium (Cs^+) is usually chosen for stability, alongside any of the mentioned halogens in the X-sites. It is already evident from the number of possible combinations of these cations and anions, that perovskites allow for high customizability when it comes to their optoelectronic properties such as band gap energies, as seen in Fig. 1.10, carrier diffusion lengths, carrier mobility and quantum-yield (QY).

In contrast to other NC lattices, LHPs have a highly ionic lattice where the A-site cations and Halide anions are weakly bound. However, because of their unique electronic structure, where the conduction and valence bands are composed of antibonding orbitals, paired with their dynamic surface chemistry, LHPs exhibit high-defect tolerance. Therefore, when treated properly, LHPs have the potential to exhibit near unity quantum yields (QYs).

1.2.2 Surface functionalization

Surface functionalization plays a pivotal role in determining the optical and electronic properties of lead-halide perovskite (LHP) nanocrystals (NCs). As previously mentioned, due to their

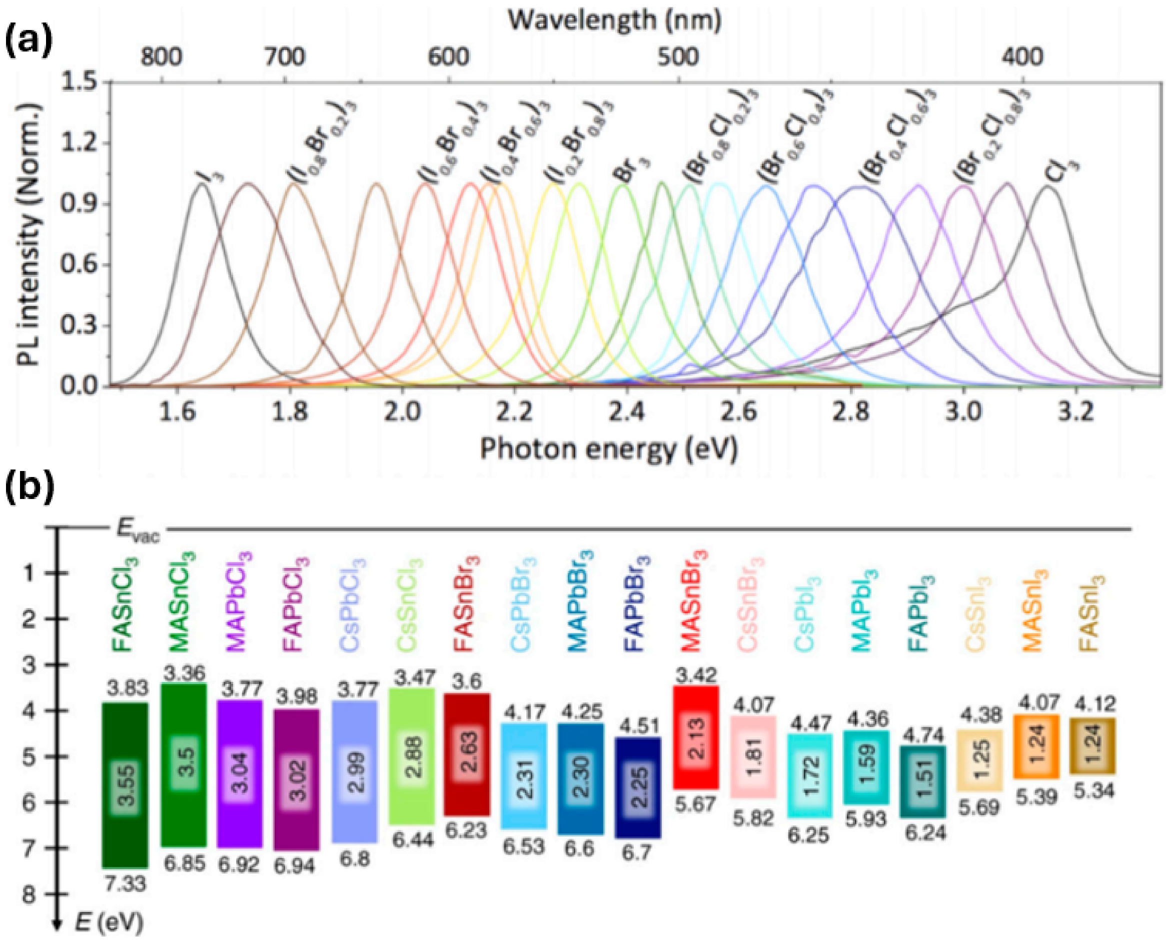

Fig. 1.10 Schematic representation of **(a)** the photoluminescence (PL) emission spectra and **(b)** the absolute energy gap values of various bulk halide perovskite crystals. Adapted from Seunghyun Rhee et al [23] **(a)** and Shuxia Tao et al [24] **(b)**.

soft ionic lattice, LHP NCs are particularly susceptible to surface defects and aggregation, which significantly limit their performance in optoelectronic applications. Effective surface passivation strategies are essential to mitigate these issues and enhance the stability, luminescence efficiency, and charge transport properties of LHP NCs.

Conventional surface passivation often employs ligands such as oleic acid (OA) and oleylamine, which, while widely used in the traditional colloidal nanocrystal families such as Cd and Pb chalcogenides, suffer from weak binding affinity, resulting in ligand loss, NC aggregation, and incomplete defect passivation. A more promising approach involves new ligand strategies customized for LHP NCs that include quaternary ammonium ligands, such as didodecyldimethylammonium bromide (DDAB). These ligands exhibit stronger binding affinity to the perovskite surface, effectively preserving the morphology and size of NCs when deposited into solid-state films. The improved binding of the ligands to the NC's surface significantly reduces the surface trap density, enhancing the photoluminescence of the NC and its radiative lifetime, by largely eliminating deep surface traps.

Further improvement has been achieved through the use of Zwitterionic ligands and even by combining DDAB ligands with metal halide complexes such as $PbBr_2$, as seen in Fig. 1.12.

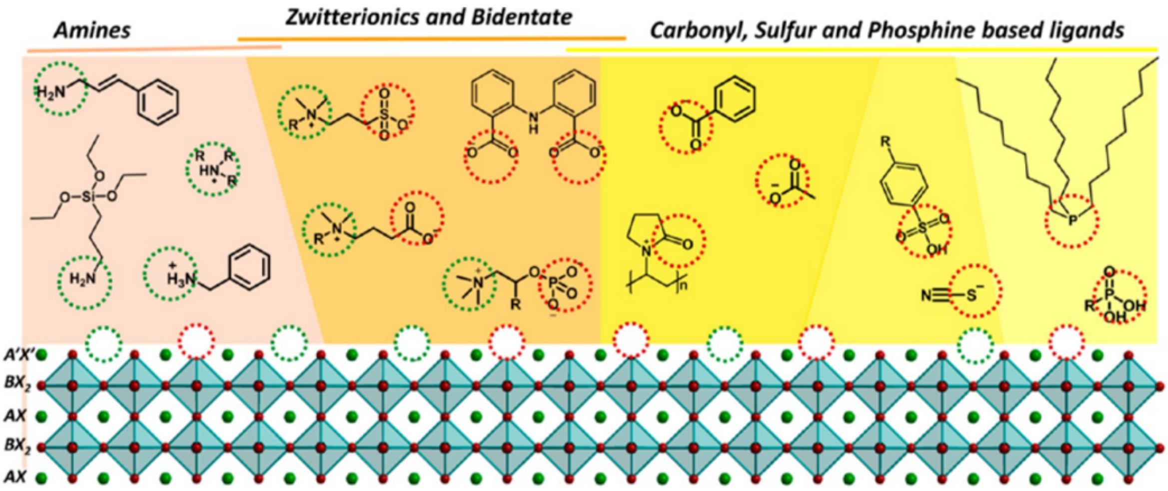

Fig. 1.11 Summary of ligands employed in surface passivation with binding at A cation sites or X anion sites. It is likely that the green-labeled functional groups occupy A sites, while the red-labeled ones occupy halide vacancies. Adapted from Fiuza-Maneiro et al. [9].

Specifically, moving from OA/Om ligands to DDAB to Zwitterionic (ZI), we observe a narrower emission spectrum (decreasing broadening Γ_0), increases of PL QYs up to 40% and increases of carrier lifetimes up to 1.5×, while the film's optical quality improves.

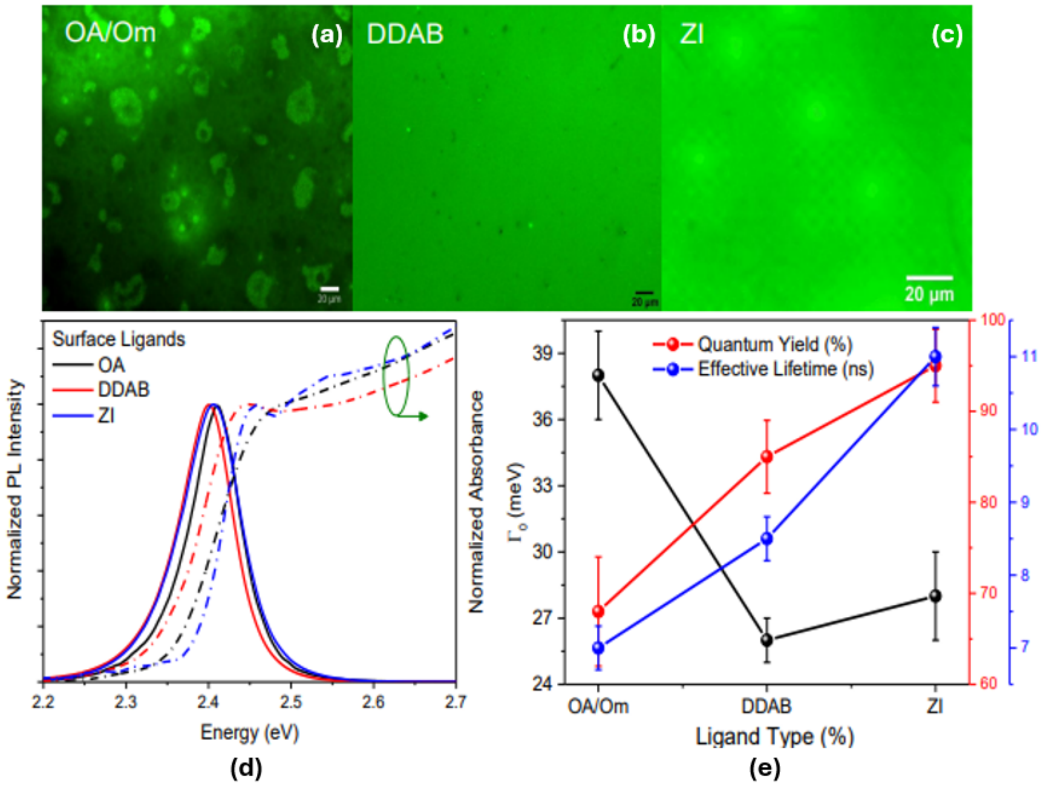

Fig. 1.12 Fluorescence microscopy images of thin films of $CsPbBr_3$ nanocrystals capped with **(a)** Oleic acid/Oleylamine ligands, **(b)** DDAB ligands, and **(c)** Zwitterionic ligands. The corresponding **(d)** normalized photoluminescence and absorption spectra and **(e)** broadening, quantum yield and carrier lifetime are also shown.

Surface passivation in LHP NCs not only enhances the optoelectronic properties of the NC, it also improves the quality of the crystal. This highlights the significance of surface treatment and ligand engineering for unlocking the full potential of LHP NCs in various optoelectronic applications, with each surface passivation strategy introducing a balance of advantages and trade-offs in the performance of the nanocrystal.

1.2.3 Impact of ligand removal

Surface ligands are essential in stabilizing colloidal NCs, especially LHP nanocrystals and maintaining their high photoluminescence quantum yield (PLQY). These ligands are typically long-chain organic molecules that passivate surface vacancies, preventing the formation of non-radiative recombination centers and minimizing surface-related trap states. As mentioned, new ligand strategies have been demonstrated for LHP NCs resulting in efficient surface passivation and preservation of strong, stable and narrow NC photoluminescence. However such effective passivation of the surface with relatively bulky molecules comes at the expense of interdot electronic interactions such as charge transport within the NC films. To improve charge transport, processes of ligand removal or exchange with smaller ligand molecules are often used. However such treatments often affect the morphological and optical properties of the NC films, as shown by Papagiorgis P. et al [19] for example.

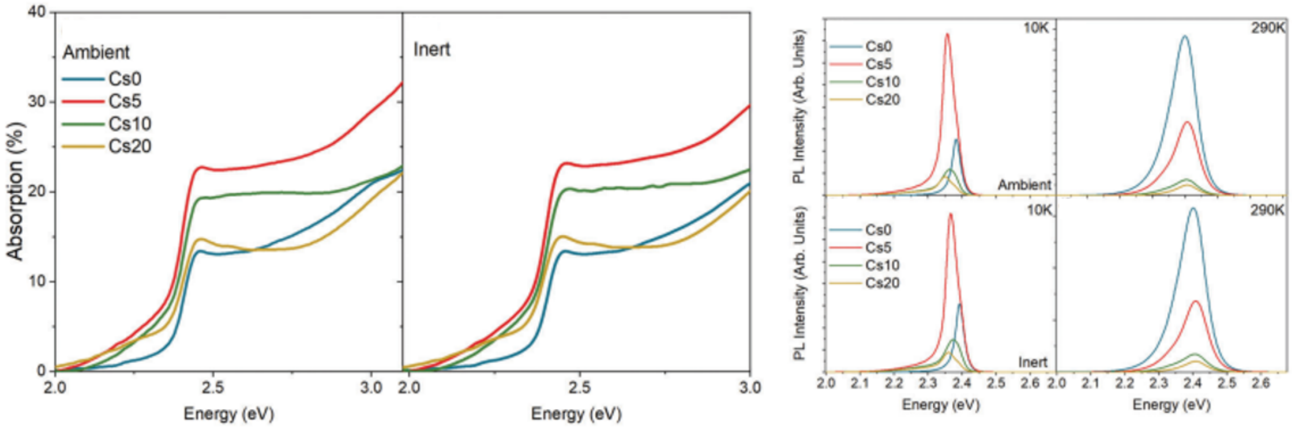

(a)

(b)

Fig. 1.13 Measured **(a)** Absorption **(b)** PL spectra for thin $CsPbBr_3$ nanocrystal films prepared in inert and ambient conditions. The notation CsX, represents the time each film was exposed to ligand washing, i.e Cs10 was washed for 10 seconds. Adapted from Papagiorgis P. et al [19].

For instance, the increased heterogenaity and not complete ligand coverage of the surface upon ligand removal introduces dangling bonds and surface states that can lead to significant broadening, and quenching of the PL spectra. These may also be accompanied by blue or red shifts in emission, caused by the degradation of surface halide sites that define the confinement conditions.

These spectral changes serve as sensitive indicators of surface integrity and are widely used to monitor the success or damage induced by ligand manipulation. While mild treatments, such as washing or partial ligand exchange, can improve nanocrystal packing and charge mobility while maintaining acceptable optical quality, aggressive ligand stripping usually results in irreversible degradation.

Chapter 2

Molecular materials

Molecular materials, characterized by discrete molecules interacting through weak intermolecular forces, exhibit distinct electronic and vibrational properties. Unlike semiconductor NCs that feature energy level quantization primarily due to spatial confinement, molecular materials have discrete electronic states, that are intrinsically determined predominantly by their molecular orbitals. Therefore, understanding their electronic structure and vibrational dynamics is essential for understanding phenomena such as charge and energy transfer in NC-Molecule heterojunctions, which are critical in applications ranging from organic electronics to molecular spintronics.

2.1 Electronic structure

The electronic structure of molecular materials fundamentally differs from that of crystalline inorganic solids. Whereas inorganic semiconductors are characterized by extended, delocalized electronic bands due to their periodic lattice structures, molecular materials typically consist of discrete molecules bound together by comparatively weak intermolecular forces such as van der Waals interactions or hydrogen bonds. Consequently, their electronic properties are predominantly determined by the molecular orbitals (MOs), specifically the highest occupied molecular orbital (HOMO) and the lowest unoccupied molecular orbital (LUMO) energies.

2.1.1 Linear combination of atomic orbitals (LCAO)

To understand the electronic structure of molecular materials, it is instructive to start from the basic principles of quantum mechanics. For a system composed of nuclei and electrons, the complete non-relativistic Hamiltonian can be written as:

$$\hat{H} = -\sum_i \frac{\hbar^2}{2m_e}\nabla_i^2 - \sum_A \frac{\hbar^2}{2M_A}\nabla_A^2 - \sum_{i,A} \frac{Z_A e^2}{4\pi\varepsilon_0|\mathbf{r}_i - \mathbf{R}_A|} + \sum_{i<j} \frac{e^2}{4\pi\varepsilon_0|\mathbf{r}_i - \mathbf{r}_j|} + \sum_{A<B} \frac{Z_A Z_B e^2}{4\pi\varepsilon_0|\mathbf{R}_A - \mathbf{R}_B|} \tag{2.1}$$

where i, j index the electrons, A, B index the nuclei, m_e and M_A are the electron and nucleus masses, Z_A is the atomic number of nucleus A, $\mathbf{r}_i$ and $\mathbf{R}_A$ are the electron and nuclear position vectors respectively and ∇ denotes the gradient operator. The terms, in order, correspond to the kinetic energy of the electrons, the kinetic energy of the nuclei, the electron-nucleus Coulomb attraction, the electron-electron Coulomb repulsion and the nucleus-nucleus Coulomb repulsion.

Evidently, the Hamiltonian is highly complex due to the coupled electron-nuclear motion. To simplify, we apply the Born-Oppenheimer approximation, which assumes that because nuclei are much heavier than electrons, their motion can be treated separately. The nuclear kinetic energy term is neglected at first, allowing us to solve for the electronic structure at fixed nuclear positions. Thus, the electronic Hamiltonian becomes:

$$\hat{H}_{\text{el}} = -\sum_i \frac{\hbar^2}{2m_e}\nabla_i^2 - \sum_{i,A} \frac{Z_A e^2}{4\pi\varepsilon_0 |\mathbf{r}_i - \mathbf{R}_A|} + \sum_{i<j} \frac{e^2}{4\pi\varepsilon_0 |\mathbf{r}_i - \mathbf{r}_j|} + V_{\text{nuclei}} \tag{2.2}$$

where V_{nuclei} is now a constant for fixed nuclear positions.

The Linear Combination of Atomic Orbitals (LCAO) approach offers a conceptual and practical method to build molecular orbitals. It is essentially an application of the Variational principle, and postulates that the wavefunction ψ of an electron in a molecule can be approximated as a sum of atomic orbitals ϕ centered on the different nuclei:

$$\psi = \sum_i c_i \phi_i \tag{2.3}$$

where c_i are coefficients to be determined by variational principles and ϕ_i are atomic orbitals (e.g., $1s$, $2p$) of the hydrogen atom. The physical meaning is that an electron in a molecule is "shared" between atoms, occupying a delocalized orbital built from atomic contributions. Substituting the LCAO expression into the Schrödinger equation and projecting onto each atomic orbital (i.e., multiplying by ϕ_j^* and integrating), leads to a matrix eigenvalue problem:

$$\hat{H}_{\text{el}}\psi = E\psi \tag{2.4}$$

$$\sum_i (H_{ji} - ES_{ji})c_i = 0 \tag{2.5}$$

where $H_{ji} = \langle \phi_j | \hat{H}_{\text{el}} | \phi_i \rangle$ is the Hamiltonian matrix element and $S_{ji} = \langle \phi_j | \phi_i \rangle$ is the overlap integral between orbitals. In short, solving this secular determinant (eq. 2.6) yields the molecular orbital energies and coefficients.

$$\det |\mathbf{H} - E\mathbf{S}| = 0 \tag{2.6}$$

A simple example is shown in Atkins P. [3], where these principles are applied to the hydrogen ion molecule. Assuming a linear combination of the ground state hydrogen ϕ_{1s} for the electron belonging to either nucleus and solving eq. 2.6, one obtains two discrete eigenvectors each corresponding to a different energy, as seen in Fig. 2.1a. The resulting eigenvectors of the system represent two states, a stable ,bonding, orbital and an unstable , antibonding, orbital. Intuitively, one can interpret the stability of these orbitals by their probability density at the center. When the electron density is greater at the center, the attractive forces from each nucleus balance one another, while simultaneously the repulsion between the nuclei is mitigated by their mutual attraction to the electron, making the molecule more stable.

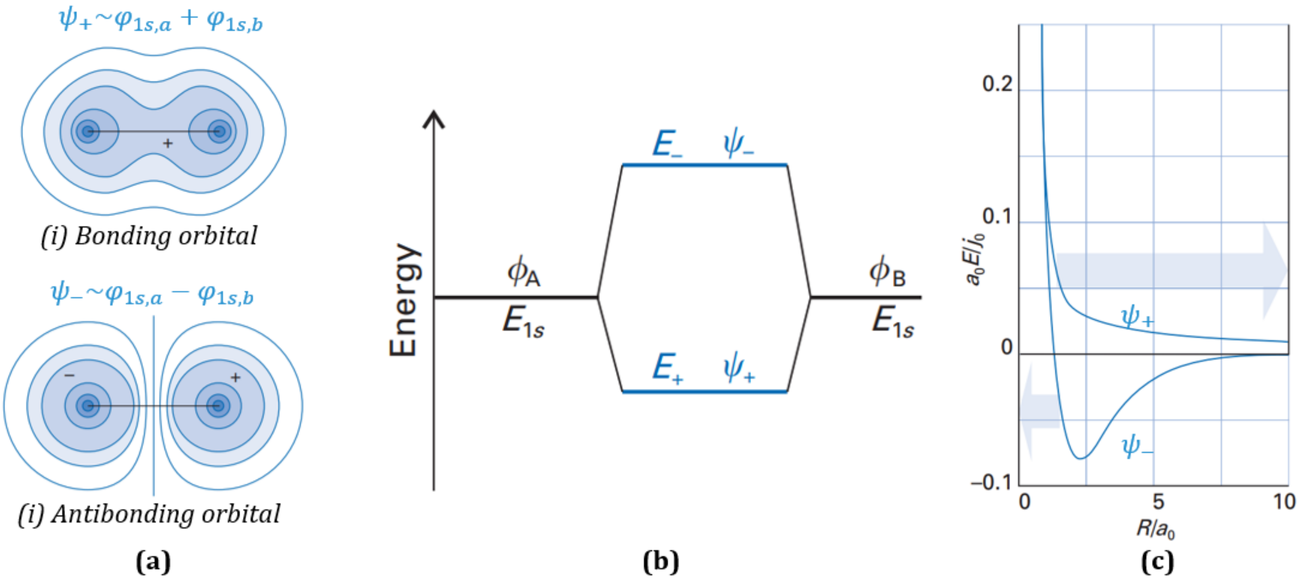

Fig. 2.1 Schematic representation of **(a)** contour plots of the probability densities of the hydrogen ion in 2D, **(b)** the the creation of two distinct energy states from linear combinations of two identical atomic orbitals and **(c)** the energy of these orbitals as a function of nucleus separation R (with $j_0 = \frac{e^2}{4\pi\epsilon_0}$ and a_0 being the Bohr radius) . Adapted from Atkins P. and Friedman R. [3].

In general, the orbitals of a molecule are formed through the linear combination of the atomic orbitals of its constituent atoms. By combining these atomic orbitals, new orbitals are created that extend over the entire molecule, allowing electrons to be shared or distributed across multiple nuclei. This process underlies the formation of chemical bonds and explains many of the electronic properties of molecules beyond simple systems like the hydrogen molecular ion.

2.1.2 Frontier orbitals

Electrons in molecules occupy discrete energy levels known as molecular orbitals (MOs), which arise from combining atomic orbitals through methods like the previously discussed Linear Combination of Atomic Orbitals (LCAO). Although a molecule possesses many such orbitals, each characterized by different energies and spatial distributions, not all orbitals equally influence the molecule's chemical, optical, or electronic properties. Instead, it is the frontier molecular orbitals, namely the Highest Occupied Molecular Orbital (HOMO), the Lowest Unoccupied Molecular Orbital (LUMO), and in radicals, the Singly Occupied Molecular Orbital (SOMO), that predominantly determine molecular reactivity, charge transport, and spectral features.

Electrons fill molecular orbitals sequentially from the lowest energy upwards, occupying each orbital with up to two electrons of opposite spin. This behavior is dictated by the Pauli exclusion principle, which states that no two electrons in a system can have identical sets of quantum numbers. As a result, each orbital can hold a maximum of two electrons with antiparallel spins.

2.1.2.1 HOMO and LUMO

The HOMO is the highest energy orbital containing electrons in the molecule's ground state, whereas the LUMO is the lowest energy orbital that is vacant, as shown in Fig. 2.2. These two orbitals form the energetic boundary between filled and unfilled states. The energy gap between them, plays a central role in determining a molecule's electronic and optical properties, such as absorption wavelengths and redox potentials.

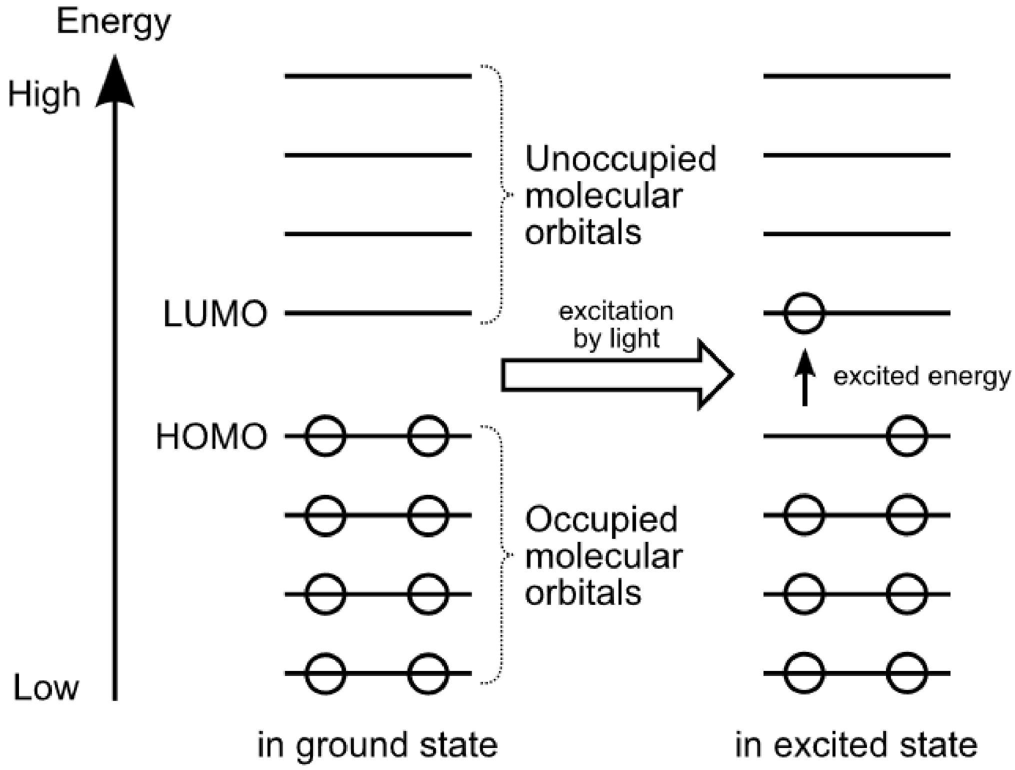

Fig. 2.2 General schematic representation of the highest occupied molecular orbital (HOMO), and lowest unoccupied molecular orbital (LUMO) of a molecule.

The HOMO is typically associated with electron donating behavior, whereas the LUMO typically acts as an electron acceptor. Optical transitions from the HOMO to the LUMO are commonly observed in UV-Vis spectroscopy, especially in conjugated systems, where the delocalization of π electrons reduces the HOMO-LUMO gap to visible wavelengths.

2.1.2.2 SOMO : The radical frontier

In radical species, which contain an odd number of electrons, the molecular orbital picture includes a Singly Occupied Molecular Orbital (SOMO). This orbital holds a single unpaired electron, distinguishing open-shell systems from closed-shell ones.

The SOMO typically lies energetically between the HOMO[1] and the LUMO and introduces unique properties, such as magnetic activity due to the unpaired spin (detectable via ESR),

---

[1] Technically, the highest energetically occupied orbital is the SOMO. For this reason, in the rest of this thesis, we will refer to the orbital just before the SOMO as HOMO-1.

possibility of optical transitions such as SOMO→LUMO, as shown in Fig. 2.3, and an increased chemical reactivity due to the presence of a half filled orbital.

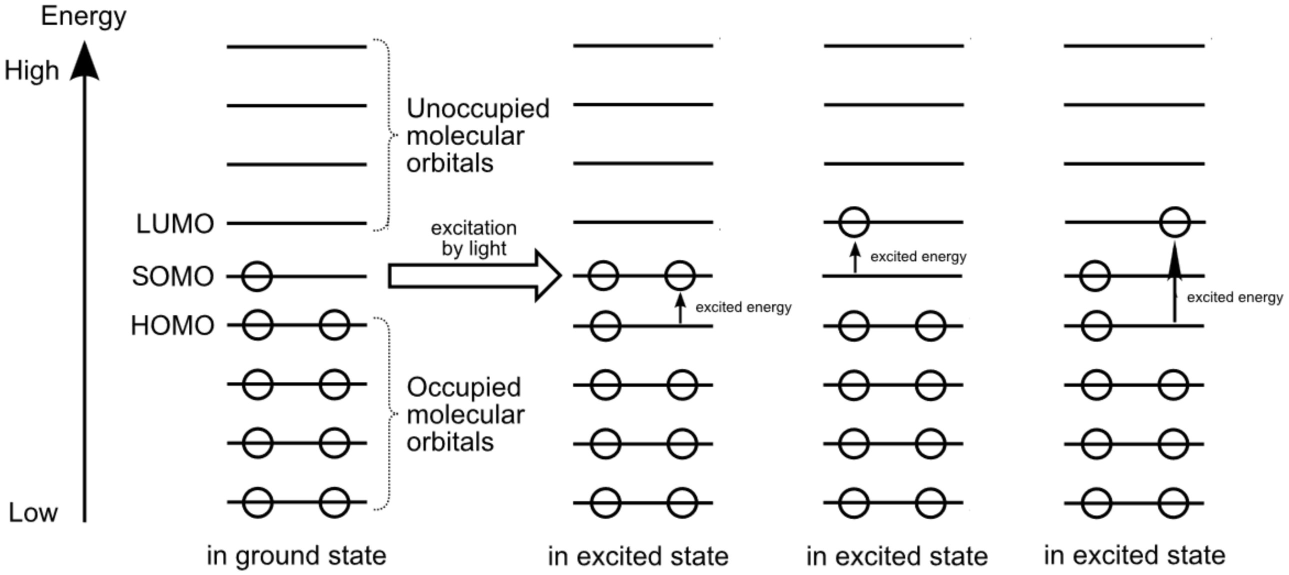

Fig. 2.3 General schematic representation of the second highest occupied molecular orbital (HOMO-1), lowest unoccupied molecular orbital (LUMO) and singly occupied molecular orbital (SOMO) of a molecule.

In hybrid materials, such as those combining organic radicals and inorganic semiconductors, the alignment of frontier orbitals at the interface determines the direction and efficiency of charge or energy transfer. For example, in a heterojunction between a radicals and nanocrystals, electronic interactions may involve the SOMO, LUMO or HOMO-1 of the radical and the conduction or valence band edges of the perovskite NC. Understanding the energies, spatial distributions, and occupancies of frontier orbitals is therefore essential for interpreting both the spectroscopy and the functionality of such hybrid nanomaterials.

2.2 Parent Blatter radical

As mentioned previously, radical species contain an unpaired electron[2] in a singly occupied molecular orbital. This makes radicals magnetically active at the cost of high reactivity, as such molecules tend to pair their extra electrons through different reactions, making them highly unstable. The parent Blatter radical however, shows a quite exceptional stability, while at the same time maintaining all the other desired properties of radicals, making it a promising contender for applications in novel spintronic and optoelectronic devices.

---

[2] In fact, some species may even have more than one unpaired electrons in different orbitals, typically referred to as SOMO, SOMO-1, SOMO-2 and so on.

2.2.1 Molecular structure

The parent Blatter radical, formally known as 1-phenyl-3-phenyl-1,4-dihydro-1,2,4-benzotriazin-4-yl, shown in Fig. 2.4, is an open-shell species, with the unpaired electron delocalized over the triazinyl ring system. Despite the presence of nitrogen atoms, which introduce some polarity, the absence of hydrogen bond-donating or strongly polar functional groups renders the molecule largely hydrophobic. This hydrophobic character influences its solubility, favoring organic solvents over aqueous environments.

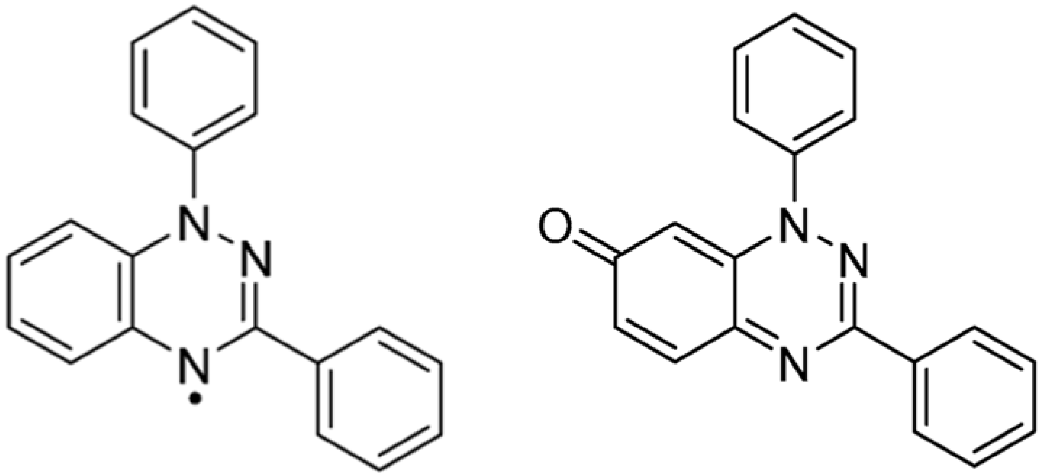

(a) **(b)**

Fig. 2.4 Molecular structure of (a) the parent blatter radical, and (b) its oxidized counterpart, Quinonimine.

In addition to the neutral Blatter radical, its oxidized counterpart, commonly referred to as Quinonimine, also plays an important role in the redox[3] chemistry of this family of molecules. Quinonimine is a closed-shell species that results from the formal oxidation of the Blatter radical, involving the removal of the unpaired electron. Its molecular structure preserves the core aromatic framework, as shown in Fig. 2.4b, but adopts a distinct electronic configuration, which can alter its optical and electronic behavior.

The molecule's inherent stability originates from its planar, benzene ring-based frame. Compared to non-symmetric, non-circular molecules, benzene rings form large planar, delocalized orbitals. Consider ethylene, shown in Fig. 2.5a, where each carbon atom is bonded to two hydrogen atoms, with a double bond between the two carbon atoms. The two 2s electrons hybridize with one of the 2p electrons to form three sp^2 bonds, also known as σ bonds, which are arranged in a plane at an angle of about 120° to each other. The other 2p electron forms a π orbital derived from the $2p_z$ atomic orbital, with wave function lobes above and below the plane defined by the nuclei of the carbon and hydrogen atoms.

---

[3] Electron transfer between two species, involving two simultaneous processes. The first is oxidation, where the donor loses electrons, increasing its oxidation state, and the second is reduction, where the acceptor gains electrons, decreasing its oxidation state.

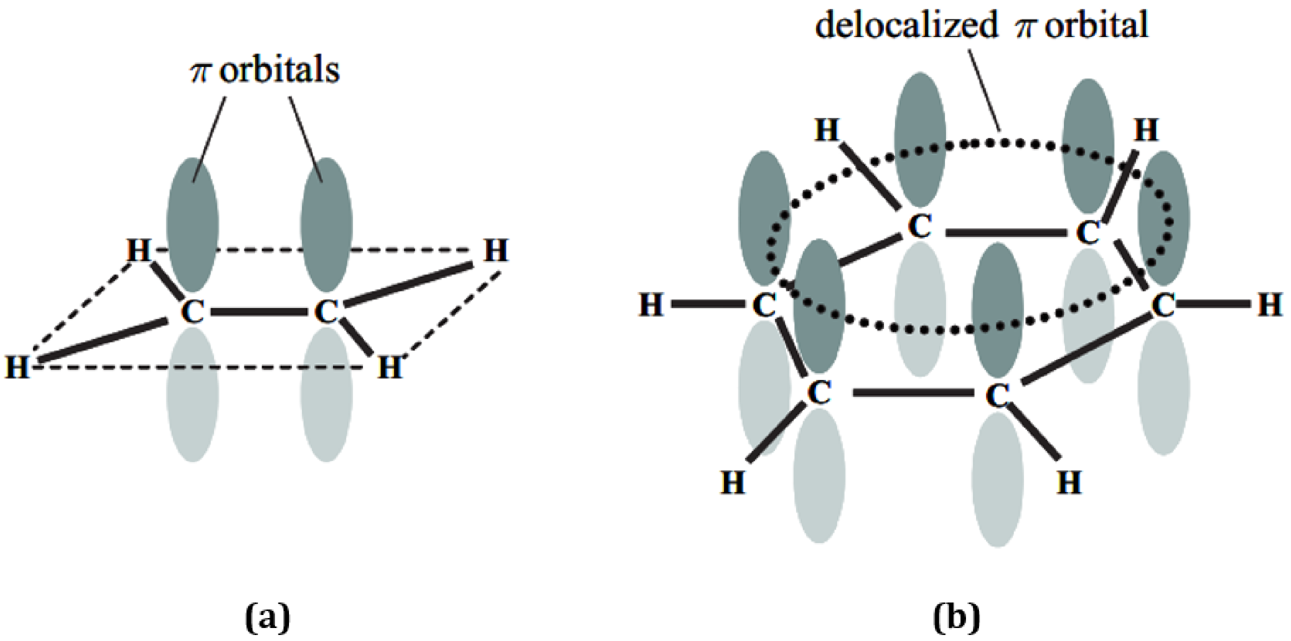

Fig. 2.5 Schematic representation of **(a)** ethylene (C_2H_4) and **(b)** benzene (C_6H_6) and their electron orbitals. Adapted from Fox M. [10].

The carbon atoms in benzene share the same sp^2 hybridization as ethylene, with each atom forming σ bonds with one hydrogen atom and its two adjacent carbon atoms. The π electrons however, now form a ring above and below the molecule, as the electrons are shared equally in the conjugated[4] bonds on either side. The spin density in this conjugated π system is therefore spread out, forming large delocalized orbitals that reduce the molecule's reactivity.

This enhanced thermodynamic stability, an uncommon property of open-shell systems, paired with the the presence of a free spin, significantly improves its practical utility, and makes this radical a promising candidate for applications in advanced materials and spintronic research.

2.2.2 Electronic and Spin Properties

The Blatter radical is a stable organic radical characterized by an unpaired electron delocalized over its conjugated π-system, particularly the triazinyl ring. This delocalization contributes to its remarkable thermal and chemical stability, distinguishing it from many other organic radicals [4].

Electron Paramagnetic Resonance (EPR) spectroscopy is instrumental in probing the spin properties of the Blatter radical. Specifically, EPR studies reveal that the unpaired electron exhibits significant delocalization, consistent with the discussion in the previous subsection, leading to narrow linewidths and hyperfine coupling patterns indicative of interactions with nitrogen nuclei within the radical core.(ref. [16])

In the context of spintronics, the Blatter radical's open-shell configuration and stability make

---

[4] Conjugated referring to the alternating multiple and single bonds between the carbon atoms.

it a promising candidate for molecular spintronic devices. When interfaced with metal electrodes, such as gold, the radical maintains its spin characteristics, exhibiting phenomena like the Kondo effect (ref. [25]). This effect arises from the interaction between the localized spin of the radical and the conduction electrons of the metal, leading to distinctive conductance features at low temperatures. Furthermore, the Blatter radical's spin properties can be modulated through chemical modifications. Substituent effects have been shown to influence the radical's redox potentials, spin distribution, and overall stability. Electron-donating groups, for instance, can enhance spin delocalization, thereby affecting the radical's electronic absorption and magnetic properties.(ref. [16])

These electronic and spin characteristics underscore the Blatter radical's potential in applications requiring stable organic radicals with tunable properties, particularly in the development of advanced spintronic materials and devices.

Chapter 3

Experimental techniques

This chapter outlines the experimental methods employed to investigate the optical and electronic properties of the $CsPbBr_3$-Blatter radical heterojunctions. The techniques described, including absorption, steady-state and time-resolved photoluminescence via time correlated single photon counting (TCSPC), form the basis for the analysis and interpretations presented in Chapter 4. These methods were selected in an attempt to probe intrinsic exciton recombination in the nanocrystal and radical components as well as intermaterial interactions that can potentially involve chemical interactions, interfacial recombination and charge/spin/energy exchange. Additionally, the procedures for sample preparation are detailed, for the reproducibility and reliability of the results.

3.1 Sample preparation

The NCs used in this study, were the prototypical $CsPbBr_3$ NC system of the LHP family, capped with mixture of OA/OAm/DDAB ligands, ensuring a quality passivation of the NC's surface. These NCs are mixed with the open or closed shell configurations of the Parent Blatter radical discussed in the previous section. Solutions of these materials, both at a fixed concentration of 5mg/ml and dissolved in toluene, were used to derive a series of diluted blend solutions at various volume ratios, in order to study how the relative ratio of NCs to the organic molecules affects its optical properties. The quantities used to derive the solutions are mentioned in table 3.1.

Volume ratio ($CsPbBr_3$: Blatter radical)	**$CsPbBr_3$ NCs** (μl)	**Blatter radicals** (μl)	**Blend volume** (μl)	**Radical content** (%)
200:1	1000	5	1005	0.49
100:1	500	5	505	1.00
50:1	250	5	255	1.96
10:1	200	20	220	9.09
5:1	150	30	180	16.67

Table 3.1 Blend volumes for different $CsPbBr_3$ NC to Blatter radical volume ratios. The same quantities were used for the $CsPbBr_3$ perovskite nanocrystal - Quinonimine heterojunction samples.

The solution samples of these blends were then diluted 50 times by adding 5μl of the undiluted blend to 245μl of toluene. The diluted blends were placed in a 350μl Quartz cuvette from Ossila (ref. [17]), and an identical cuvette containing 250μl of toluene was used as a reference sample for the absorption spectra, to account for the cuvette's and solvent's contributions.

Thin films were also derived from the undiluted blends[1] via spin coating. A standard model Ossila spin-coater (ref. [18]), shown in Fig. 3.1a, was used to coat 60μl of the blend solutions onto glass (BK7) substrates. Prior to deposition, the substrates were thoroughly cleaned and coated with a silane compound[2], to improve the quality and homogeneity of the films.

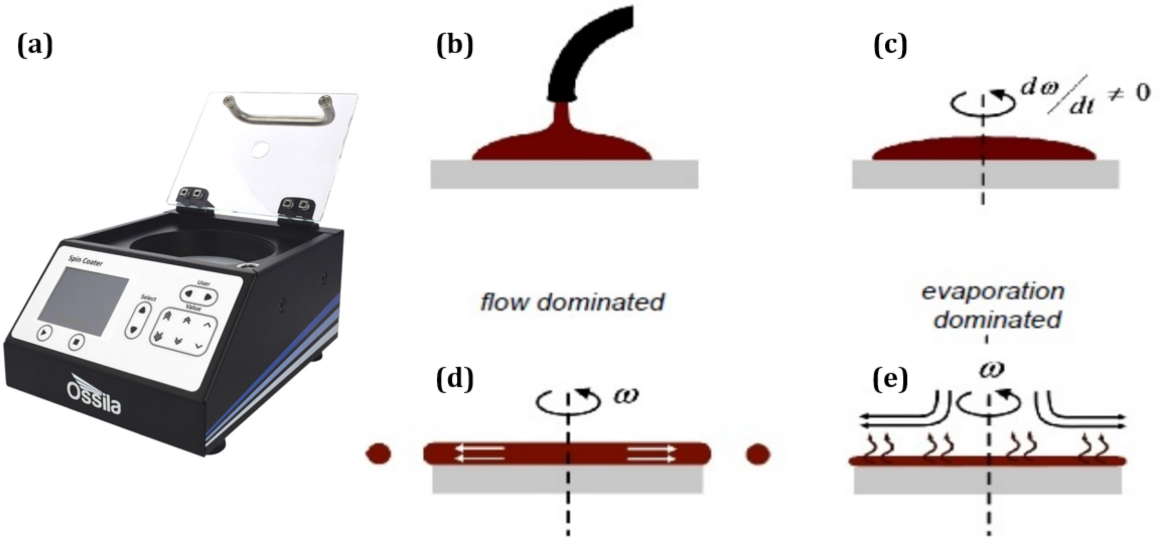

Fig. 3.1 Image of **(a)** a standard model Ossila spin coater, and schematic representation of the steps taken for thin film derivation. Namely **(b)** deposition of the material solution, **(c)** Spin up step, **(d)** Spin off step and **(e)** solvent evaporation step.

The process begins by placing a small amount of the material solution on the substrate (either while spinning or stationary). As the substrate spins, centrifugal force spreads the liquid outward, expelling most of it and forming a thin film. During the spin off phase, the film thins further due to viscous forces, and interference colors may appear as an indicator of thickness. In the final evaporation stage, solvent evaporates, solidifying the film. In this study, the films were derived using a spin up - spin off step at 1000rpm for 1 minute, followed by an evaporation step at 3000rpm for 30 seconds. The final film thickness is influenced by the solution's viscosity, spin speed, and solvent volatility.

---

[1] Keeping the original concentration of the blend allowed for thicker films, improving the detected signals in our measurements.

[2] LHP nanocrystals, alongside their ligands, as well as the open and closed shell blatter radicals, are in general hydrophobic. The BK7 glass substrates however are hydrophilic, as their surface contains hydroxyl (-OH) groups that can form bonds with water. By treating the surfaces with silane, non-polar organic groups (e.g. -CH_3) replace the hydroxyl groups, making the surface hydrophobic, allowing for more uniform, high quality films derived from hydrophobic materials

3.2 Optical spectroscopy

To probe the photophysical behavior of the $CsPbBr_3$-Blatter radical heterojunctions, a series of optical spectroscopy techniques were employed. These methods, ranging from absorption and steady-state photoluminescence to time-resolved measurements, allow for detailed characterization of light-matter interactions and dynamic processes such as exciton recombination and charge transfer. The following subsections describe the principles and procedures of each technique used in this study.

3.2.1 Absorption

The optical absorption spectra were recorded using a Perkin-Elmer Lambda 1050 spectrometer (ref. [21]), shown in Fig. 3.2, which operates by comparing the intensity of a reference light beam with that transmitted through the sample. The instrument employs two light sources: a deuterium lamp (200-320 nm) for UV and a tungsten lamp (300-3250 nm) for visible to NIR wavelengths. These sources pass through a monochromator that selects a specific wavelength using a double diffraction grating and focusing mirrors.

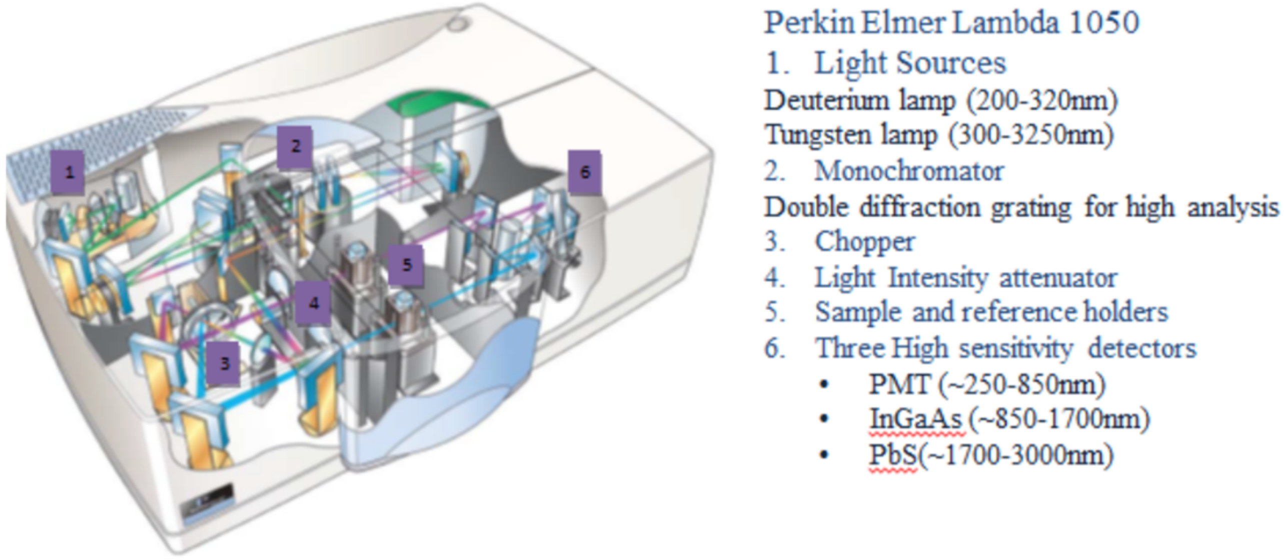

Fig. 3.2 Schematic of the PerkinElmer Lambda 1050 spectrophotometer's component parts. Adapted from PerkinElmer [21]

The resulting monochromatic beam is split into two paths, one for reference and one through the sample, as shown in Fig. 3.3. Detectors including a PMT (250-850 nm), an InGaAs sensor (850-1700 nm), and a PbS sensor (1700-3000 nm) measure transmitted light intensitY, I_T, across the full spectral range. A lock-in amplifier enhances signal-to-noise by isolating the modulated signal corresponding to the sample's absorption.

The absorbance of the material is then calculated using the Beer-Lambert law, from the measured optical density (O.D), as expressed by equations 3.1 and 3.2.

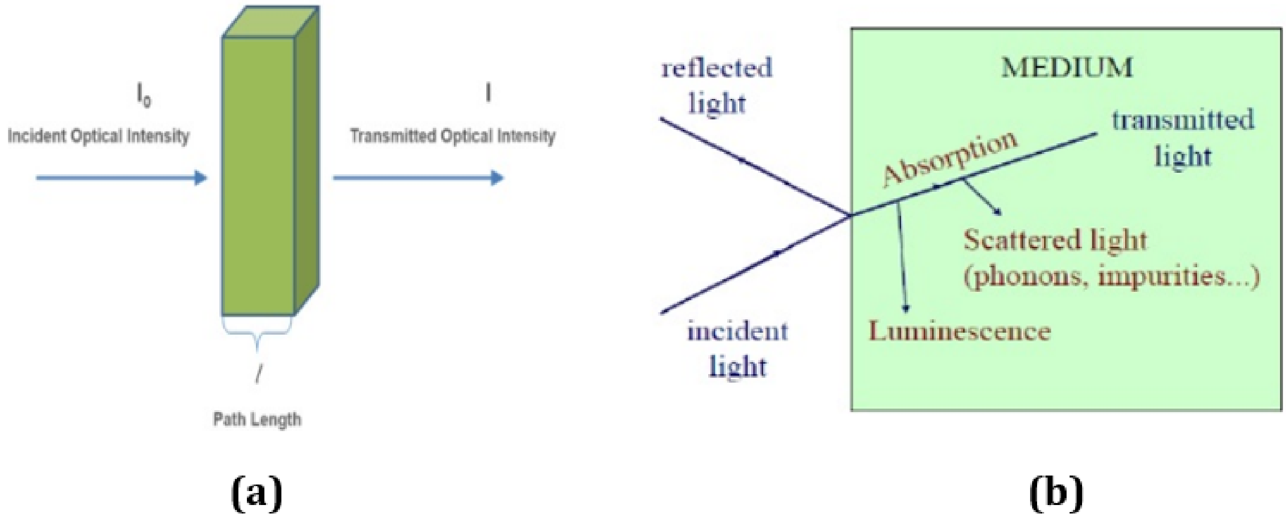

Fig. 3.3 Schematic of **(a)** Beer-Lambert's law and **(b)** the processes that take place during a measurement. Adapted from Fox M. [10].

$$\text{O.D.} = -\log_{10}\left(\frac{I_T}{I_0}\right) \tag{3.1}$$

$$A = 1 - \frac{I_T}{I_0} = 1 - 10^{-\text{O.D.}} \tag{3.2}$$

3.2.2 Photoluminescence (PL and PLE)

The photoluminescence (PL) and excitation photoluminescence (PLE) spectra were acquired using a modular Fluorolog FL3 Horiba spectrophotometer (ref. [7]), as shown in Fig. 3.5. The system utilizes a high power, stabilized EQ-99X-QZ-S laser driven light source (LDLS) from Hamamatsu (ref. [13]) as an excitation source. A constant flow of nitrogen in the plasma chamber allows for emission of deep UV wavelengths and providing sufficient power output across a large range of wavelengths (170-2400 nm), as shown in Fig. 3.4, by displacing the oxygen that would otherwise absorb the UV light creating ozone in the chamber.

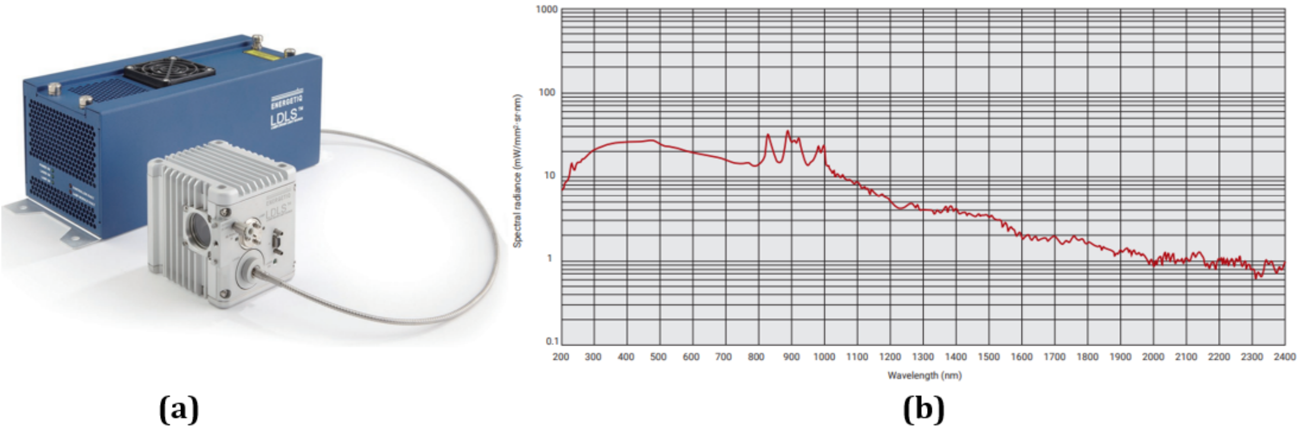

Fig. 3.4 Image of **(a)** the model EQ-99X-QZ-S LDLS, and **(b)** the corresponding spectral radiance. Adapted from Hamamatsu Photonics K.K [13].

The white light emitted by the plasma is filtered through a high-resolution double monochromator containing two 1200 g/mm holographic gratings, with a reference Si-diode at the lamp's exit monitoring fluctuations in the source's intensity. Samples are placed in a dedicated chamber, shown in Fig. 3.5, and emission is collected either at a right angle geometry. Emitted light is directed through an iHR32 spectrometer with a triple-grating turret and detected by either a visible-range TBX photomultiplier tube (250-850 nm) or a Hamamatsu infrared detector (95-1700 nm). For our studies only the visible detector was used. The system allows for standard PL as well as PLE measurements, the latter performed by scanning the excitation wavelength while monitoring emission at a fixed wavelength, to probe emissive transitions in the material.

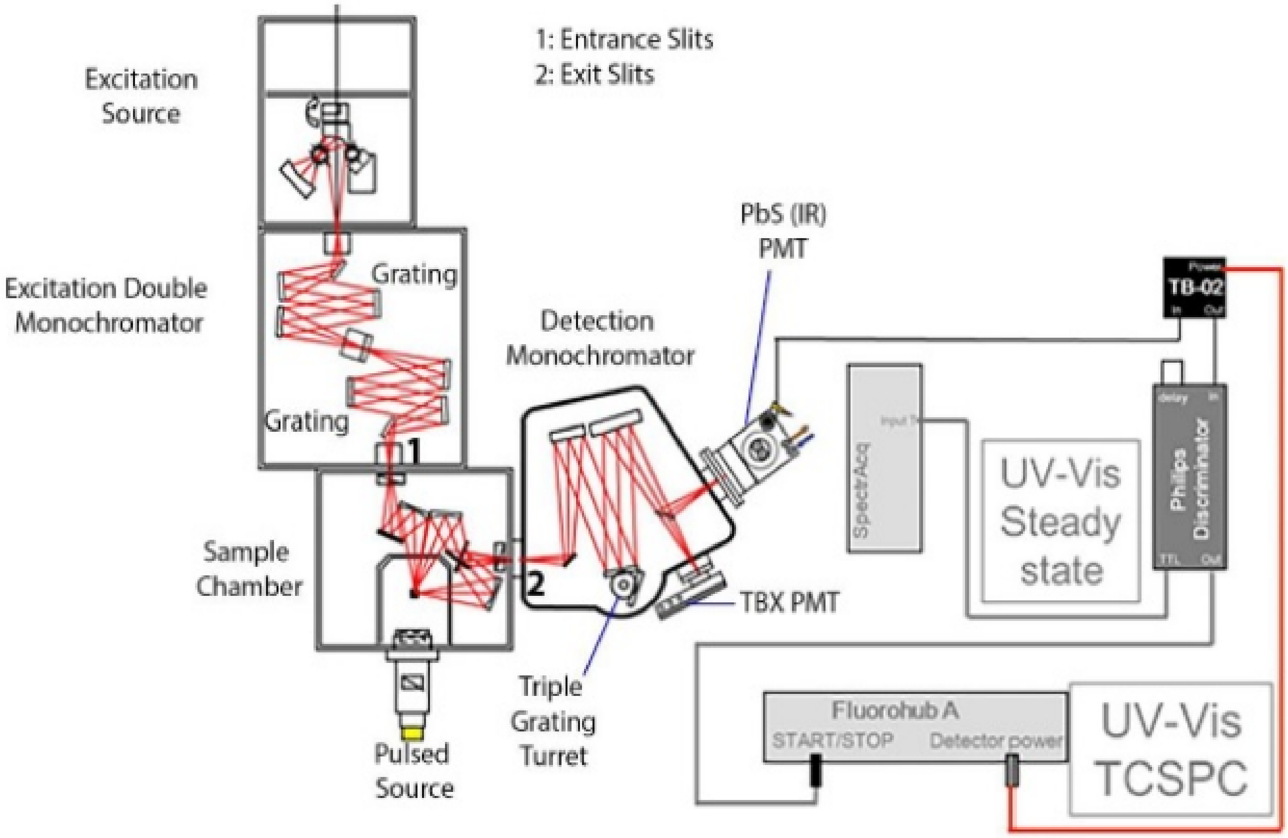

Fig. 3.5 Schematic of the modular Fluorolog FL3 Horiba spectrophotometer's component parts. Adapted from Cohen M. S. [7].

3.2.3 Photoluminescence Quantum Yield (PLQY)

Photoluminescence quantum yield (PLQY or η) is a crucial metric in assessing the emission efficiency of semiconducting nanocrystals, defined as the ratio of emitted to absorbed photons. In this work, PLQY was determined using an integrating sphere-based method that enables absolute quantification, independent of sample geometry or emission directionality.

The experimental setup comprised an integrating sphere coated internally with a highly reflective and diffusive material (reflectivity $> 95\%$) over a broad spectral range (300-1400 nm). The sample was positioned at the center of the sphere, as shown in Fig. 3.6c, mounted on a holder with rotational and vertical adjustability, ensuring isotropic light distribution and effective capture of both direct and indirectly scattered emission. A baffle was strategically placed to prevent direct detection of either the excitation source or the sample luminescence, ensuring that only multiply scattered light was collected. To determine the PLQY, three distinct spectral measurements were conducted:

1. **Reference Spectrum (L_a):** Recorded with the empty sphere to measure the integrated intensity of the excitation source.
2. **Indirect Excitation Spectrum (L_b and P_b):** Obtained with the sample in the sphere but positioned outside the excitation beam's direct path. This records residual laser light and photoluminescence induced by scattered excitation.
3. **Direct Excitation Spectrum (L_c and P_c):** Captured with the sample in the excitation beam path, measuring both the reduced excitation intensity and directly excited photoluminescence.

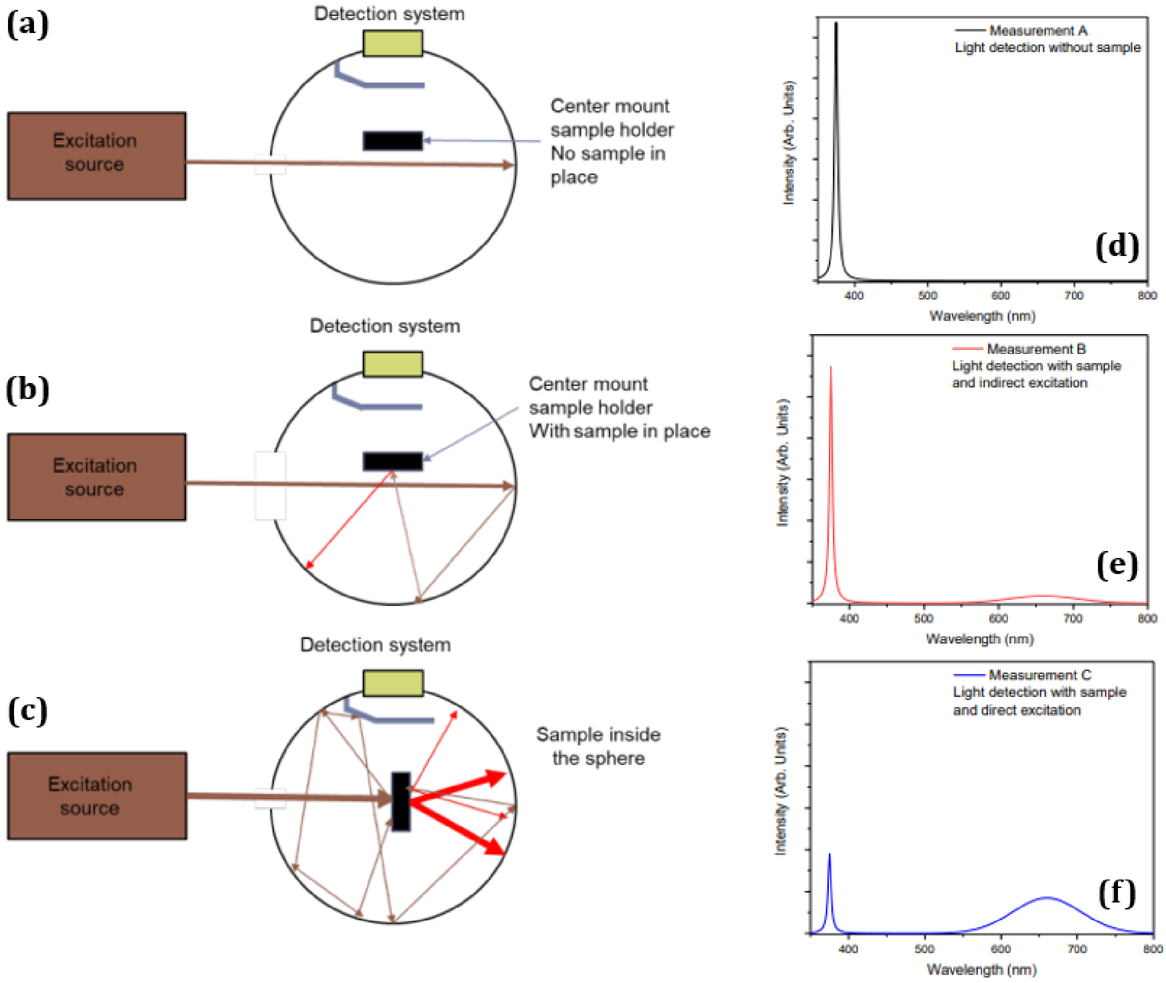

Fig. 3.6 Schematic representation of the three experimental configurations for the QY measurement. In the first **(a)** the excitation source spectrum **(d)** is measured in the absence of a sample. The second measurement's setup **(b)** records the spectrum of indirect excitation emission of the sample along with the excitation's source light. The third geometry **(c)** measures the spectrum **(f)** under direct excitation of the sample. Adapted from Papagiorgis P. [20].

From these spectra, the absorbed excitation light was calculated as:

$$A = 1 - \frac{L_c}{L_b}$$

and the quantum yield was derived using the relation:

$$\eta = \frac{P_c - (1 - A)P_b}{L_a A}$$

where P_c and P_b represent the integrated PL emission under direct and indirect excitation, respectively. This method, allows for accurate, reproducible evaluation of PLQY, even in samples with low absorption or directional emission profiles.

3.2.4 Time correlated single photon counting (TCSPC)

The time resolved photoluminescence (TRPL) spectra were measured using the time correlated single photon counting method (TCSPC), which measures the time delay between a pulsed laser excitation and the detection of the first emitted photon from the sample. A schematic of the setup is shown in Fig. 3.7. In this technique, a picosecond pulsed laser diode excites the sample repeatedly, and the emission events are recorded by a fast photomultiplier tube (PMT) detector.

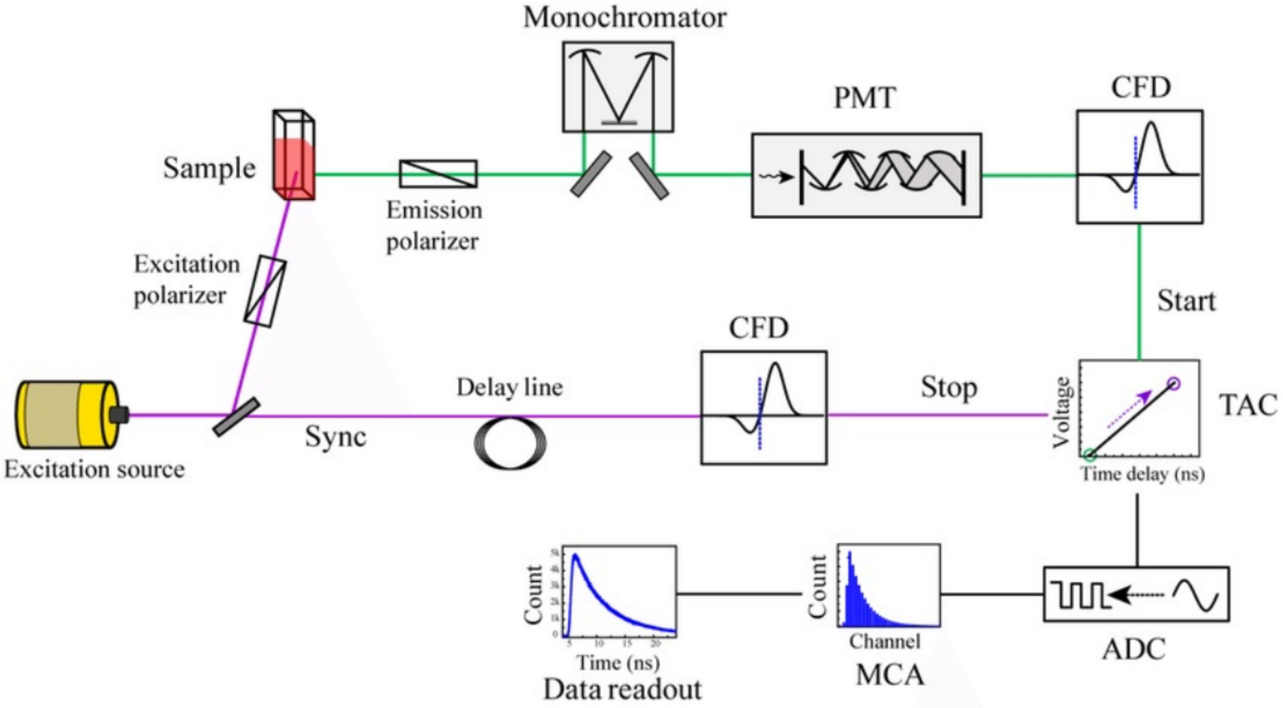

Fig. 3.7 Schematic of TCSPC method, employed for measuring the TRPL spectra of our samples.

Each detection event is time-stamped relative to the excitation pulse, and over many repetitions, a histogram of photon arrival times is built, representing the decay of luminescence. The sensitivity and temporal resolution of the technique allows us to study a plethora of the dynamics of recombination processes in the sample and extract important information such as the radiative exciton lifetime, Auger recombination, trapping or charge transfer rates and more.

The histogram recorded by TCSPC can typically be described by single or multi-exponential decay fits, that provide estimates of the rates of the various carrier and exciton recombination channels. In our TCSPC experiments, the histogram is typically modeled using a multi-exponential decay function of the form :

$$I(t) = y_0 + \sum_{i=1}^{n} A_i e^{-t/\tau_i} \tag{3.3}$$

where A_i and τ_i are the amplitude and lifetime of each decay channel, and y_0 is a background offset. By normalizing the amplitudes ($\sum A_i = 1$), one can compute the weighted contributions of each channel. The effective lifetime, τ_{eff}, is derived using:

$$\tau_{\text{eff}} = \frac{\sum A_i \tau_i^2}{\sum A_i \tau_i} \tag{3.4}$$

Chapter 4

Discussion of results

This chapter presents and interprets the data gathered from the optical spectroscopy of $CsPbBr_3$ perovskite nanocrystals (NCs), capped with a mixture of OA/OAm/DDAB ligands, and their heterojunctions with Blatter radicals. Based on the theory and methodologies established in the previous chapters, the photophysical behavior of the hybrid systems is analyzed in the steady-state and time-resolved regime. Particular focus is given to how the interaction between the NCs and the open- and closed-shell organic systems influences the photoluminescence quenching, exciton dynamics, and intermaterial transfer mechanisms. The discussion integrates data from absorption, photoluminescence (PL), time-correlated single photon counting (TCSPC), and transient absorption spectroscopy, for a comprehensive evaluation of the NC-radical interface and its implications for hybrid optoelectronic and spintronic applications.

4.1 Optical properties of Pristine $CsPbBr_3$ Perovskite NCs

To begin with, the basic optical properties of $CsPbBr_3$ Perovskite NCs, in the form of colloids and thin films are measured. These specific NCs are cubic, with side lengths of ∼10nm, and are capped with a mixture of OA/OAm/DDAB ligands, ensuring quality passivation of the NC's surface. The measured absorption, PL and TRPL spectra, of 5mg/ml NC solutions and thin films are shown in Fig. 4.1, alongside representative fluorescence microscopy images of the samples under UV light. Similar spectral characteristics are observed for both films and solutions, with a peak absorption centered at ∼505nm and an emission centered at ∼513nm, corresponding to a NC gap of 2.39eV.

Comparatively, the absorption coefficient of the SC film is greater, as the solvent is evaporated during the film deposition, leaving a much higher concentration of absorbing species compared to the dynamic environment of the solution.[1] Additionally, the PL spectra of the SC film is

---

[1] It should also be noted that in the cuvettes used, the path length for a solution is large, typically 1 cm. For a film, the path length is determined by the film thickness, which is much smaller, of the order of 100nm (10^{-4} cm), but the effective absorbance per unit volume is higher due to increased density of NC absorbers.

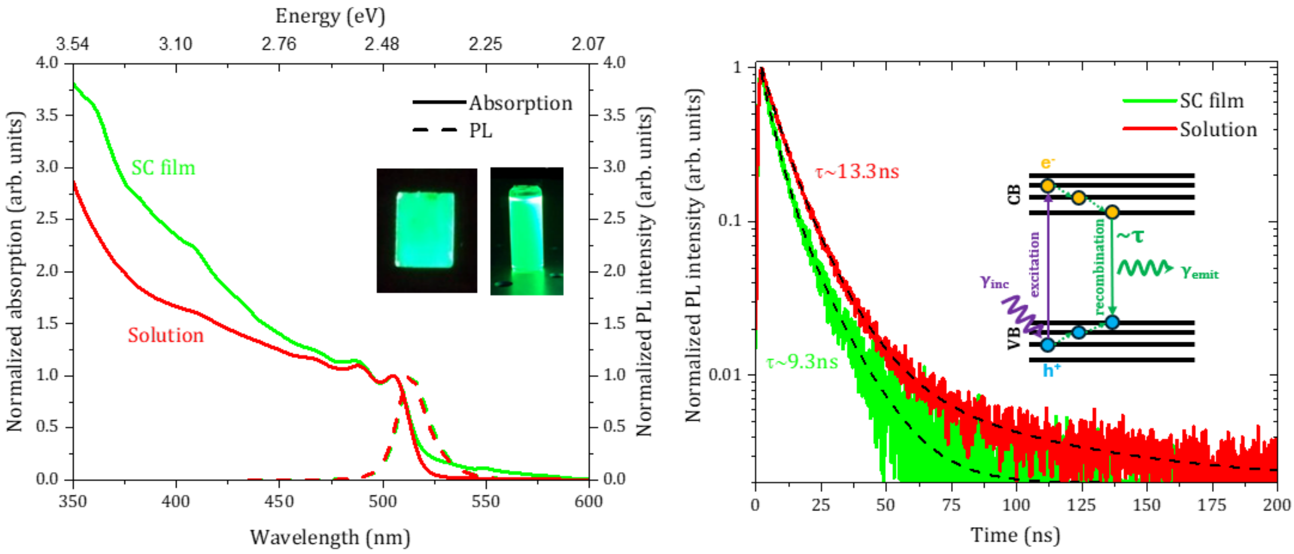

(a) **(b)**

Fig. 4.1 Measured **(a)** absorption and photoluminescence spectra, with a 400nm wavelength excitation source and a 435nm long pass filter at the exit. The time-resolved photoluminescence spectra of the NC's emission at 513nm, **(b)**, were measured using a 401nm wavelength laser excitation source with the same long pass filter at the exit.

ever so slightly (∼1nm) redshifted compared to the solution, as the electronic states of the NCs are more delocalized in the solid-state, due to close packing, leading to lower energy transitions. Radiative exciton recombination appears to be faster in the SC film, as suggested by the TRPL spectra of Fig. 4.1. This is a common observation, due to the increased disorder in the solid state combined with electronic communication between NCs due to the increased delocalization of the exciton wavefunction stated above, causing an overall faster exciton recombination.[2]

The VB and CB energy level values with respect to the vacuum level were calculated using Ultraviolet photoelectron spectroscopy (UPS) by Liu Y. et al [15], as shown in Fig. 4.2, at -5.8eV and -3.4eV for the VB and CB respectively. The estimated bandgap is consistent with the experimentally observed emission of our nanocrystals.

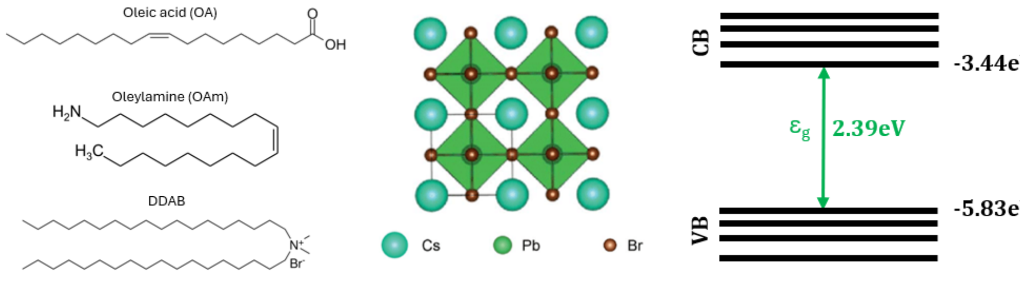

(a) **(b)** **(c)**

Fig. 4.2 Molecular structure of **(a)** the ligands used for passivation of the NC's surface, and **(b)** crystal structure of $CsPbBr_3$ NCs with **(c)** their respective energy levels.

---

[2] The dense NC packing in films and the more extended NC exciton wavefunction, can lead to quenching pathways such as exciton-exciton annihilation and exciton or charge transfer within neighboring NCs, shortening the PL lifetimes.

4.2 Optical properties of the open and closed - shell systems

In addition to the blatter radical's robust chemical stability, optically, it exhibits characteristic absorption spanning both ultraviolet (UV) and visible spectral regions. One notable feature of the optical absorption and emission spectra of Blatter radicals is the appearance of structured bands, particularly in the visible region. These features often manifest as a series of peaks or shoulders superimposed on the broad electronic transition. This fine structure is indicative of vibronic coupling, the interaction between electronic transitions and specific molecular vibrational modes. Specifically, prominent absorption bands are observed near 272 nm, and less intense features appear around 322, 370, 427, 492, and a weak absorption at approximately 554nm, as shown in Fig. 4.3a, and mentioned in Karecla et al [12].These absorption features correspond to electronic transitions involving the radical's frontier molecular orbitals, as measured computationally, using time-dependent density functional theory (TD-DFT), as shown in Fig. 4.4 and referenced in table 4.1 for the open-shell system, and table 4.2 for the closed shell system.

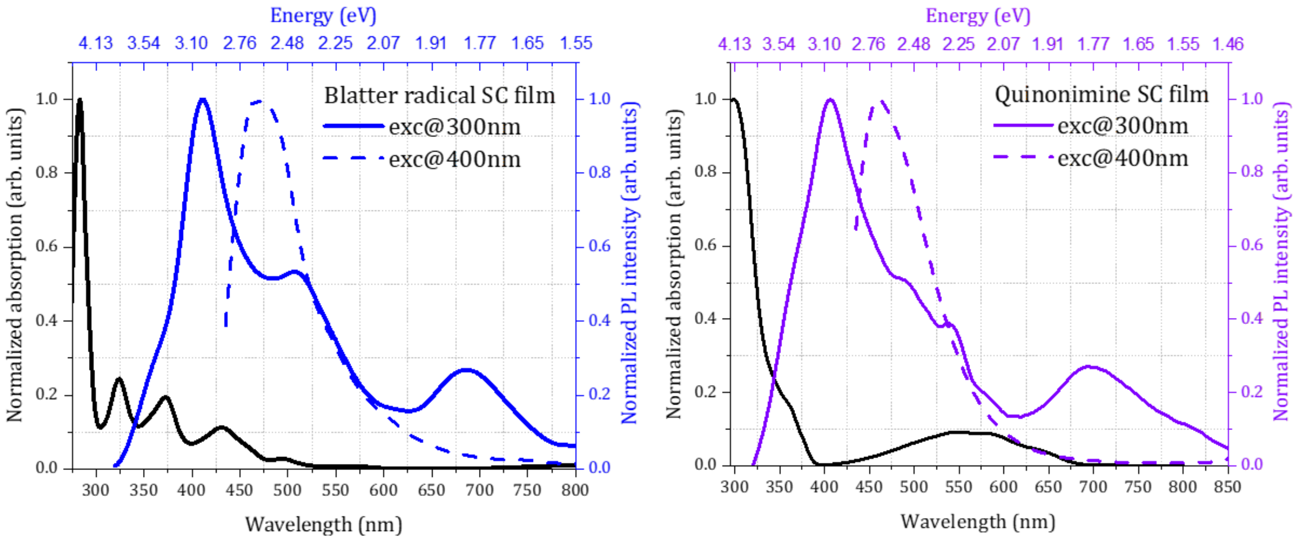

(a) **(b)**

Fig. 4.3 Experimentally measured absorption and photoluminescence spectra for thin films of **(a)** the parent blatter radical and **(b)** and its oxidized counterpart, Quinonimine.

The oxidized form of the Blatter radical, Quinonimine, typically lacks the pronounced vibronic structure observed in the radical's absorption spectrum. This is because Quinonimine is a closed-shell system, and its electronic transitions involve less geometric reorganization and weaker vibronic coupling. As a result, its absorption bands are broader and more featureless, especially in polar solvents or at room temperature. Despite the significant differences in their absorption spectra, the photoluminescence spectra of the two species remain remarkably similar in shape. It should be noted however, that the spectra are normalized for comparison reasons but the actual overall emission coming from the closed-shell system is much weaker than the one from the open-shell system.

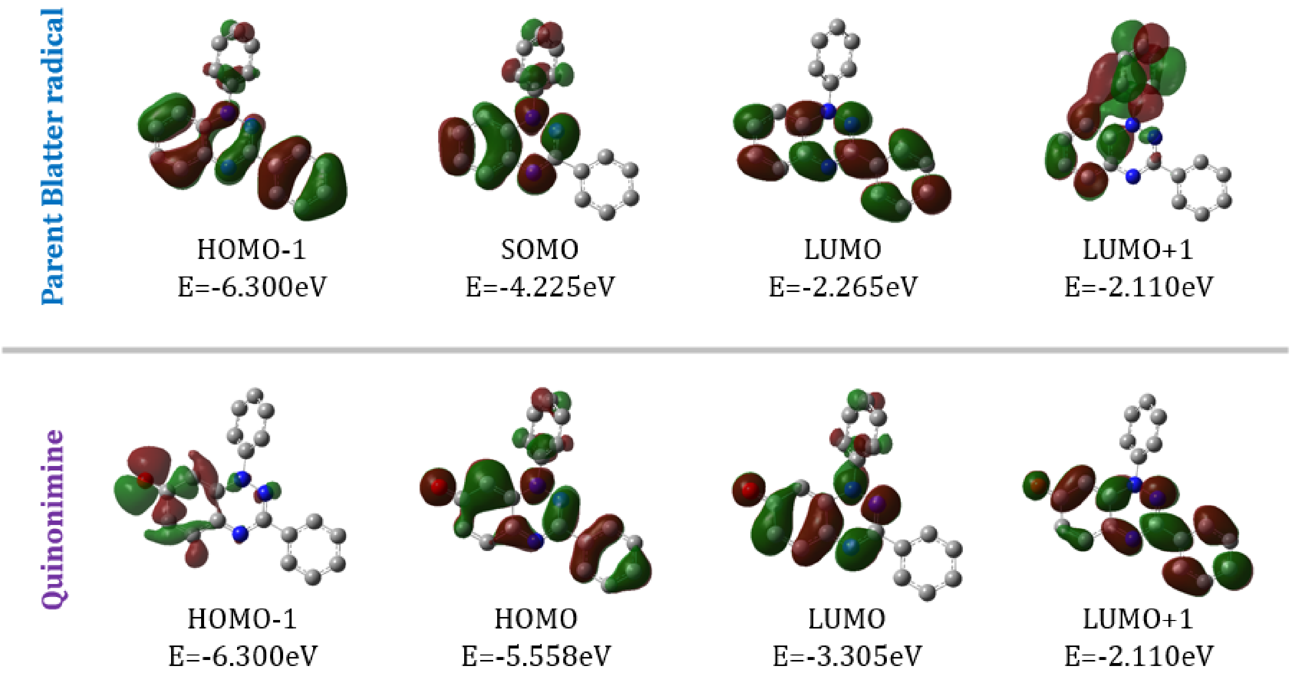

Fig. 4.4 Computationally measured orbitals and the corresponding spin densities for the open-shell parent blatter radical, and the closed-shell Quinonimine.

Excited State	**Transition (%)**	**Energy (eV)**	**Wavelength (nm)**	**f**
1	SOMO(α)$\rightarrow$LUMO(α) (95)	2.1525	575.99	0.0014
2	SOMO-1(β)$\rightarrow$SOMO(β) (76)	2.6162	473.91	0.0137
4	SOMO(α)$\rightarrow$LUMO+1(α) (83)	2.9600	418.86	0.0696
5	SOMO(α)$\rightarrow$LUMO+2(α) (93)	3.2620	380.09	0.0051
6	SOMO-4(β)$\rightarrow$SOMO(β) (25) SOMO-3(β)$\rightarrow$SOMO(β) (14) SOMO-2(β)$\rightarrow$SOMO(β) (34)	3.3138	374.14	0.0331
8	SOMO(α)$\rightarrow$LUMO+3(α) (49)	3.5198	352.25	0.0156
10	SOMO(α)$\rightarrow$LUMO+3(α) (20) SOMO-5(β)$\rightarrow$SOMO(β) (15)	3.7913	327.02	0.0732
14	SOMO-5(α)$\rightarrow$LUMO+2(α) (18) SOMO-6(β)$\rightarrow$SOMO(β) (33)	4.1254	300.54	0.0232
18	SOMO-4(α)$\rightarrow$LUMO(α) (17) SOMO-4(β)$\rightarrow$LUMO(β) (20)	4.3156	287.3	0.0138

Table 4.1 Selected electronic transitions and properties of the open-shell system, the parent blatter radical, and the corresponding oscillator strengths (f), as measured computationally using TD-DFT by Koutentis A. P. et al [6].

Excited State	**Transition (%)**	**Energy (eV)**	**Wavelength (nm)**	**f**
1	HOMO→LUMO (75)	2.254	550.1	0.0776
2	HOMO-1→LUMO (93)	2.399	516.9	0.0003
3	HOMO-7→LUMO (12) HOMO-6→LUMO (38) HOMO-4→LUMO (26) HOMO-3→LUMO (14)	3.428	361.7	0.0031
4	HOMO-3→LUMO (12) HOMO-2→LUMO (78) HOMO→LUMO+1 (8)	3.449	359.5	0.0001
5	HOMO-6→LUMO (10) HOMO-4→LUMO (6) HOMO-3→LUMO (60) HOMO-2→LUMO (16) HOMO→LUMO+1 (4)	3.491	355.2	0.0033
6	HOMO-7→LUMO (6) HOMO-6→LUMO (7) HOMO-5→LUMO (20) HOMO-4→LUMO (52)	3.759	329.9	0.1793
7	HOMO-6→LUMO (20) HOMO-5→LUMO (15) HOMO-4→LUMO (57)	3.900	317.9	0.0157
8	HOMO-7→LUMO (52) HOMO-5→LUMO (36)	3.981	311.5	0.0557
9	HOMO-1→LUMO+1 (89)	4.146	299.0	0.0022
10	HOMO→LUMO+2 (88)	4.157	298.3	0.0416

Table 4.2 Selected electronic transitions and properties of the closed-shell system, Quinonimine, and the corresponding oscillator strengths (f), as measured computationally using TD-DFT by Koutentis A. P. et al [6].

4.3 Characterization of NC-Organic molecule hybrid samples

We now concentrate in examining the optical properties of the peroskite NCs when mixed with the parent Blatter radical. In the pristine NCs and at high nanocrystal-to-radical ratios (200:1 and 100:1), the photoluminescence excitation (PLE) spectra closely track the absorption spectra[3], indicating that all absorbed photons efficiently contribute to the radiative recombination of the photogenerated NC excitons. This overlap suggests minimal disruption to exciton dynamics, with energy relaxation pathways largely funneling into the NC emissive states. However, as the radical concentration increases (ratios of 50:1, 10:1, and 5:1[4]), a clear divergence between the PLE and absorption spectra emerges. While absorption assumes a similar spectral shape, the PLE becomes increasingly attenuated at higher excitation energies corresponding to

---

[3] This is typical in pristine films of nanocrystals with well-passivated surfaces, as non-radiative losses are minimal and there is only one primary emission

[4] While it may appear that the PLE spectrum tracks the absorption spectrum more closely than the 50:1 and 10:1 samples, this should be interpreted with caution. Due to the significantly reduced emission intensity, the excitation slits had to be widened to collect sufficient signal, which affects the spectral resolution. This adjustment also caused the earlier cutoff of the PLE spectrum relative to the other samples.

NC excited states or the so-called hot excitons. This behavior implies that the blatter radicals introduce quenching mechanisms, that reduce the radiative recombination efficiency of such hot excitons..

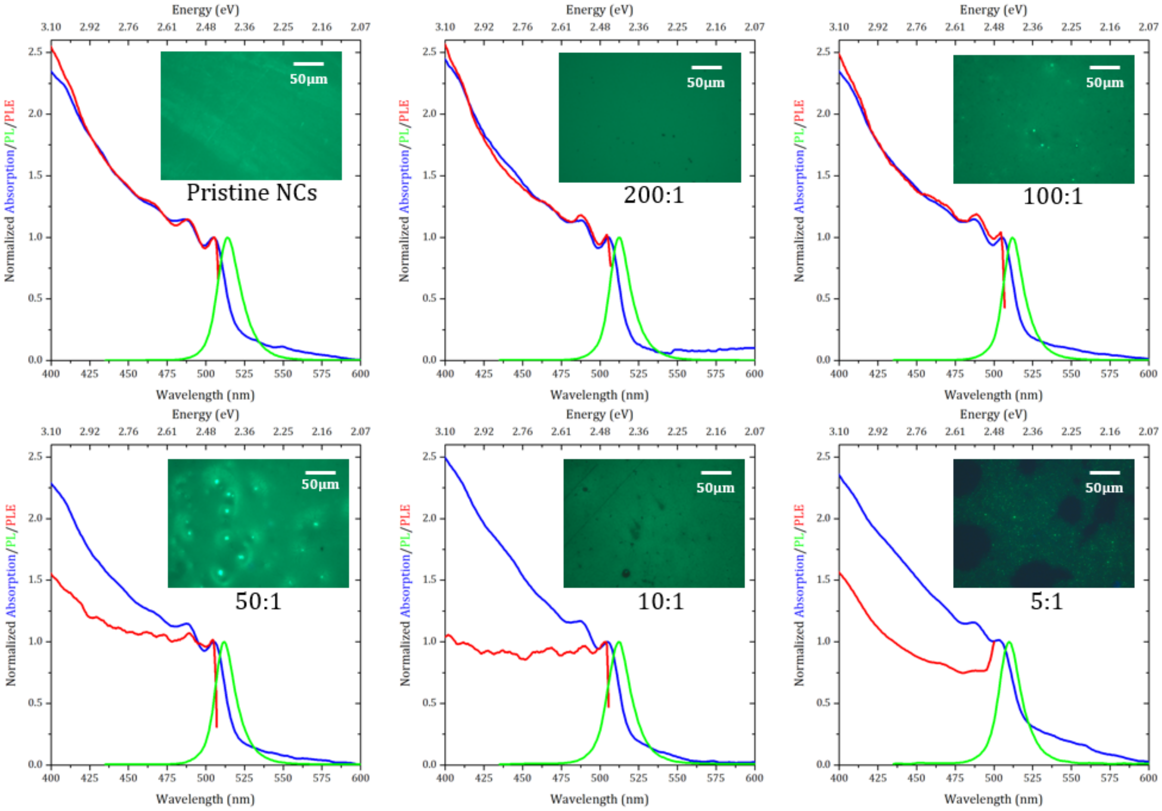

Fig. 4.5 Measured Absorption, PL and PLE spectra of the thin, SC films derived from the Perovskite nanocrystal - Blatter radical blend solutions of table 3.1, normalized and overlayed, alongside fluorescence microscopy images of the samples.

These spectral changes are accompanied by reduced morphological quality and uniformity of the thin films, as seen in the corresponding optical microscopy images. In particular, the pristine and 200:1 and 100:1 films appear smooth and continuous with bright, uniform luminescence under UV excitation. However, as radical loading increases, the films become increasingly heterogeneous, with visible aggregation, dark regions, and non-uniformity in emission.

4.3.1 Heterojunctions with Open-Shell Blatter Radicals

To assess the impact of open-shell radical molecules on the optical properties of CsPbBr3 nanocrystals, we first examine the absorption spectra of blends incorporating increasing amounts of the parent Blatter radical. No shift is observed in the primary NC exciton peak, centered at 505 nm, suggesting that the structural and electronic properties of the nanocrystals remain largely intact upon blending with the radical molecules.

As the radical content increases, subtle absorption features attributable to the Blatter radical begin to emerge but remain relatively faint. This is primarily due to the fact that the radical's prominent vibronic modes appear below 430nm[5], precisely the region where the nanocrystal absorption is strongest, masking some of the finer features of the radical absorption. By increasing the radical content up to 50% (i.e., a 1:1 volume ratio), its contribution becomes more discernible and radical absorption features can be observed more clearly.

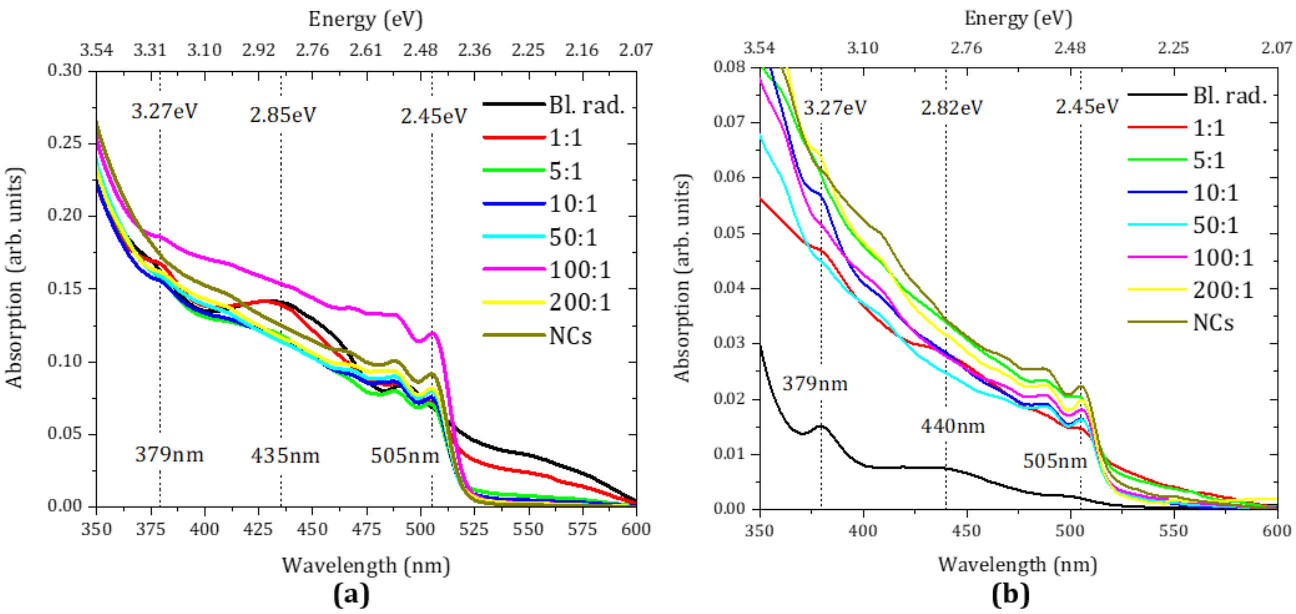

Fig. 4.6 Measured absorption spectra for **(a)** solutions and **(b)** thin SC films of blends of $CsPbBr_3$ nanocrystals and blatter radicals. A cuvette with toluene and a glass (BK7) substrate were used as references in these measurements.

Furthermore, the blend photoluminescence spectra, shown in Fig. 4.7, of the blend samples reveal a progressive quenching of the nanocrystal emission with increasing radical content. An excitation wavelength of 400nm was used for these measurements, targeting the strong absorption by the nanocrystals while remaining off resonance for the radicals. This ensured that the observed emission originates primarily from the nanocrystals, as no other emission feature was observed. While the spectral position and shape of the emission peak remain largely unchanged, as seen in Fig. 4.7b,c, suggesting minimal perturbation to the core electronic structure, the overall intensity drops notably, especially in the solid state samples, indicating the emergence of nonradiative pathways.

In addition to the reduction in intensity, a slight blue shift up to $\sim 4nm$ is observed in the emission peak as radical content increases. This trend, though modest, may indicate changes in the local dielectric environment or weak surface interactions that subtly modify the exciton recombination energy, rather than actual NC size or shape modification. On the other hand, the full width at half maximum (FWHM) of the emission exhibits non-systematic variations, suggesting that bleding of the NCs with the radical do not have a systematic impact on the NC size distribution and structural integrity.

---

[5] A vibronic mode exists around 575nm, as suggested by table 4.1, but the specific transition is weak, as implied by the small oscillator frequency.

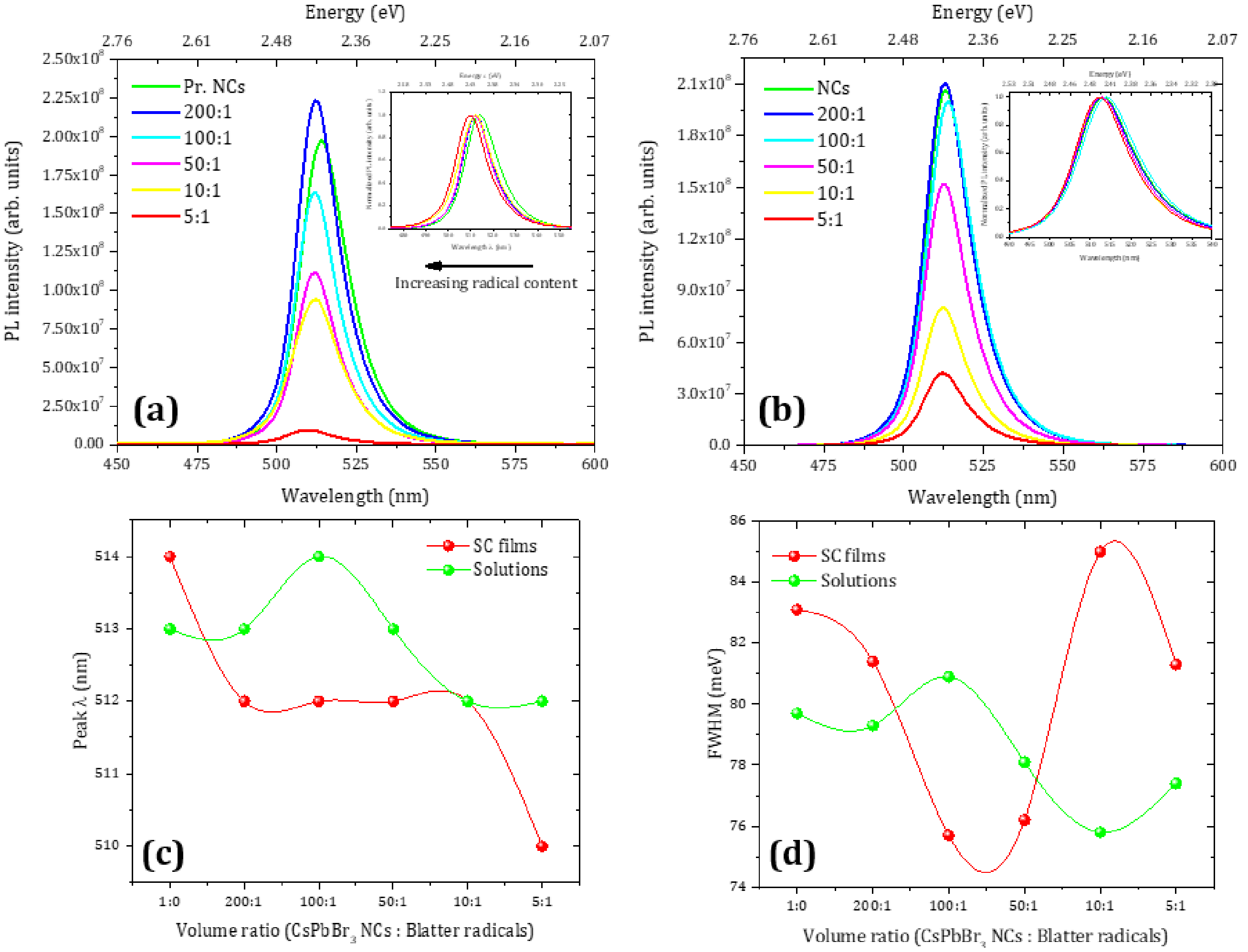

Fig. 4.7 Measured photoluminescence spectra for **(a)** solutions and **(b)** thin SC films of blends of CsPbBr$_3$ nanocrystals and blatter radicals. The spectra were corrected with the corresponding absorption of each sample at the excitation wavelength. The characteristics of the emission features, **(c)** peak center and **(d)** FWHM were also estimated.

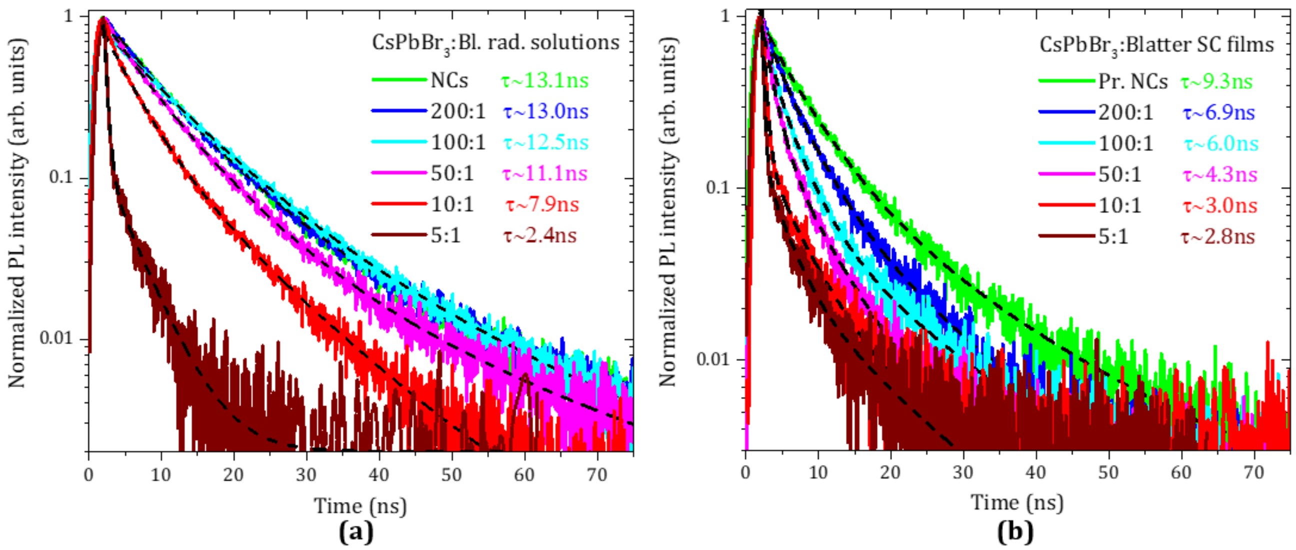

Fig. 4.8 Measured time-resolved photoluminescence spectra for **(a)** solutions and **(b)** thin SC films of blends of CsPbBr$_3$ nanocrystals and blatter radicals, normalized and overlayed, with detection at 513nm and excitation at 400nm via laser. Multi-exponential fits were performed using the Levenberg-Marquardt least-squares algorithm.

The time-resolved PL decays provide deeper insight into the recombination underlying the observed PL quenching. The measurements, shown in Fig. 4.8, reveal a clear trend of monotonic radiative exciton lifetime quenching as radical content increases, indicating enhanced nonradiative recombination in consistency with the steady-state PL results. Notably, the PL lifetime quenching is quite smaller in the blend solutions, with the exemption of the 5:1 blend, indicating an influence of the NC-radical packing on the NC exciton quenching mechanism.

4.3.2 Heterojunctions with Closed-Shell Quinonimine Molecules

To isolate and understand the role of the unpaired electron, or more specifically the singly occupied molecular orbital (SOMO) of the blatter radical in the observed interactions, blends of $CsPbBr_3$ nanocrystals with Quinonimine, the closed-shell, oxidized counterpart of the Blatter radical were also studied. By comparing these samples to the open-shell radical blends, we aim to probe the role of the SOMO radical level on the observed interactions.

Similarly to the radical-based blends, the excitonic peak of the CsPbBr3 nanocrystals, located at approximately 505nm, remains clearly visible across all blend ratios with the quinonimine compoind, with a modest decrease in intensity as Quinonimine content increases. This attenuation likely arises from increased background absorption and minor interfacial effects, rather than significant structural or electronic modification of the nanocrystals. The absorption features associated with Quinonimine, particularly those appearing above 550nm, gradually become more pronounced with increasing concentration, but they do not appear to overlap or interfere strongly with the nanocrystal excitonic transition. The spectra overall suggest weak or negligible ground-state electronic coupling between the two components, and instead point toward additive behavior, consistent with a primarily interfacial interaction.

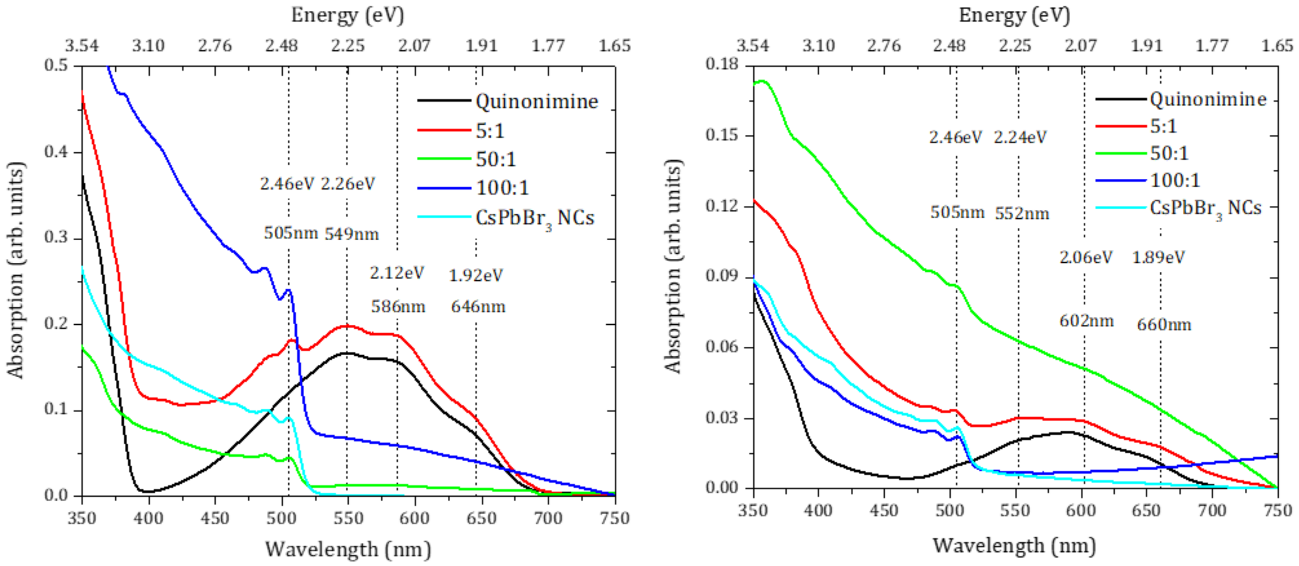

(a)
(b)

Fig. 4.9 Measured absorption spectra for **(a)** solutions and **(b)** thin SC films of blends of $CsPbBr_3$ nanocrystals and Quinonimine molecules. A cuvette with toluene and a glass (BK7) substrate were used as references in these measurements.

As in the case of the radical-based blends, a quenching of the nanocrystal photoluminescence intensity is observed for the Quinonimine-based blends, both in solution and in solid-state. However as elabrated further in the 4.3 section, where such steady-state emission reduction is more accurately determined via PL QY measurements, the quenching appears less efficient in the case of the closed shell system hybrids. On the other hand similar trends in the variation on the peak and FWHM of the NC emission are obtained for the two types of blends as evidenced by comparison of the relevant Fig. 4.10c,d and Fig. 4.7c,d. The similar blue shift of the PL peak upon incorporation of the two organic materials in the heterojnunctions, indicate as most probable origin the variation in the dielectric environment of the nanocrystals. On the other hand there is no significant variation of the PL FWHM variation that would indicate the presence of strong chemical interactions or NC degradation when mixed wiith the molecular materials.

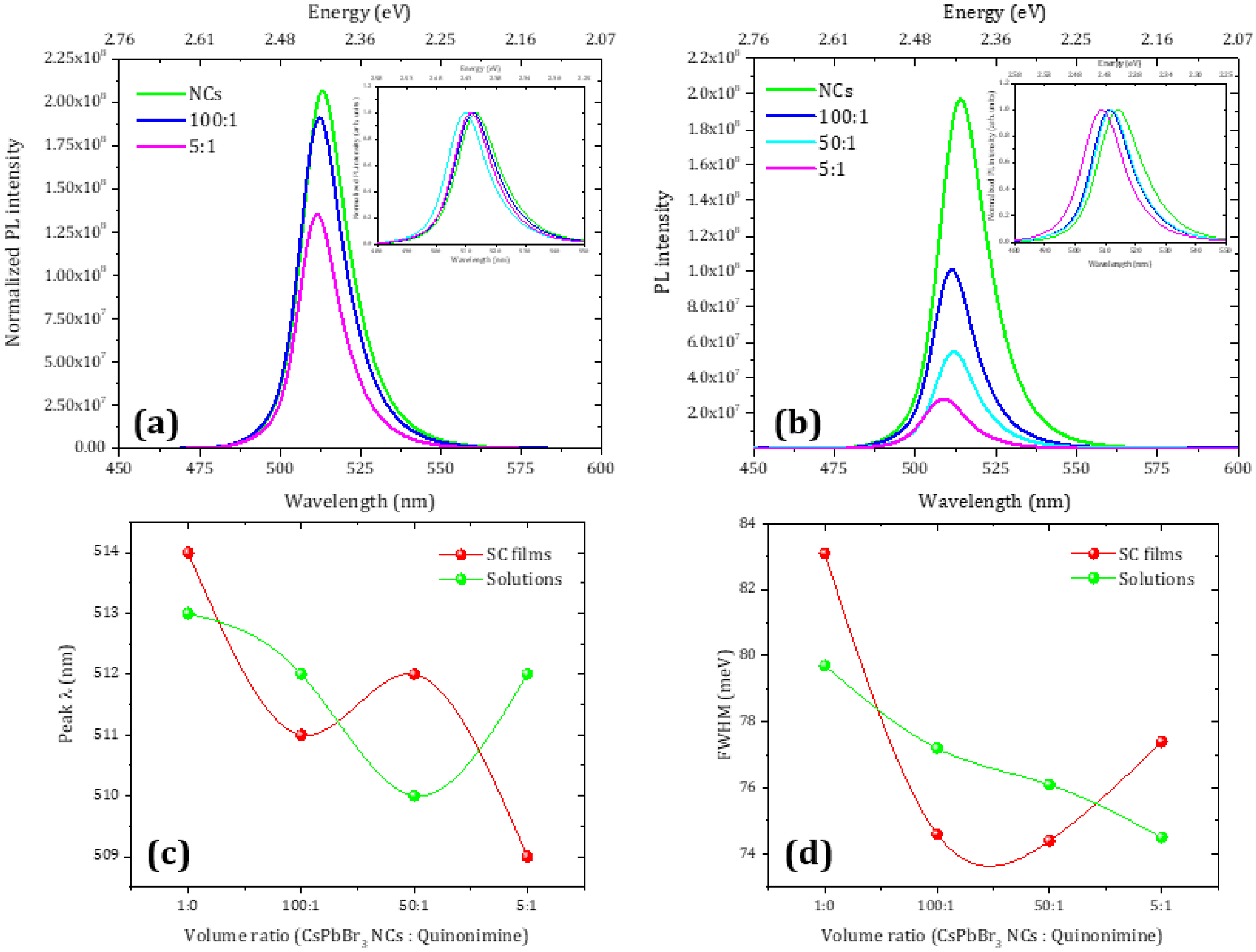

Fig. 4.10 Measured photoluminescence spectra for **(a)** solutions and **(b)** thin SC films of blends of $CsPbBr_3$ nanocrystals and Quinonimine molecules. The spectra were corrected with the corresponding absorption of each sample at the excitation wavelength. The characteristics of the emission features, **(c)** peak center and **(d)** FWHM were also estimated.

More insight is provided by the time-resolved photoluminescence (TRPL) measurements on the Quinonimine blends that reveal a different trend compared to the one observed in the Blatter radical based heterojunctions. As shown in Fig. 4.11, while there is a reduction in exciton lifetime relative to pristine nanocrystals, particularly in solid-state films, the trend is clearly not monotonic with increasing Quinonimine content. Instead, the lifetimes appear to fluctuate within a narrow range, with no clear correlation to the molecule-to-NC ratio. In solution, lifetimes remain relatively long (∼13-15 ns) for most blends, with only a modest decrease observed at the highest Quinonimine concentration (5:1). In films, a similar plateauing behavior is seen, with all blends showing lifetimes in the 5.7-6.1 ns, being reduced by the same fraction i.e. ∼35% compared to the pristine NC lifetime.

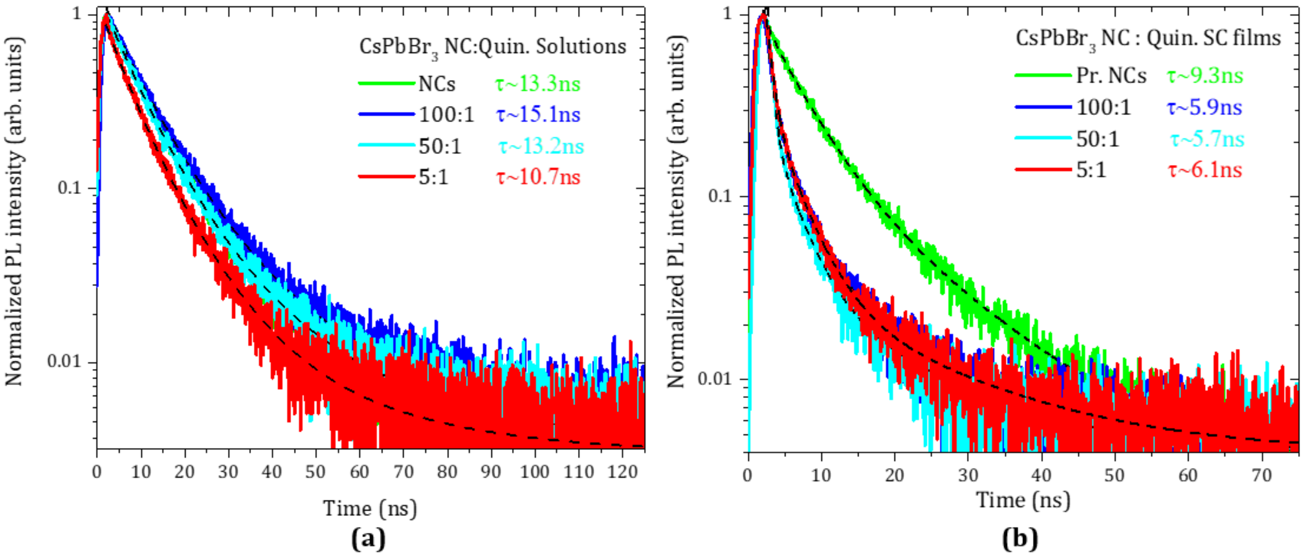

Fig. 4.11 Measured time-resolved photoluminescence spectra for **(a)** solutions and **(b)** thin SC films of blends of $CsPbBr_3$ nanocrystals and blatter radicals, normalized and overlayed, with detection at 513nm and excitation at 400nm via laser. Multi-exponential fits were performed using the Levenberg-Marquardt least-squares algorithm.

4.4 Interpretation

Comparative analysis of the optical properties of the $CsPbBr_3$ NC heterojunctions with the open-shell (Blatter radical) and the closed-shell (Quinonimine) molecules reveals both similarities and key distinctions, hinting that the radical SOMO level actively participates in the NC exciton quenching. Observations from the PLQY and relative quenching plots, shown in Fig. 4.12, indicate significant and concentration-dependent photoluminescence (PL) quenching accompanied by a marked systematic decrease in exciton lifetime for the open-shell heterojunctions. Specifically, even at just 1% Blatter radical content, the PLQY of blend films already experience a notable decrease from approximately 95% to 64%, with a corresponding PL lifetime quenching of ∼34%.

Increasing radical content amplifies this effect dramatically, reaching PLQY values as low as

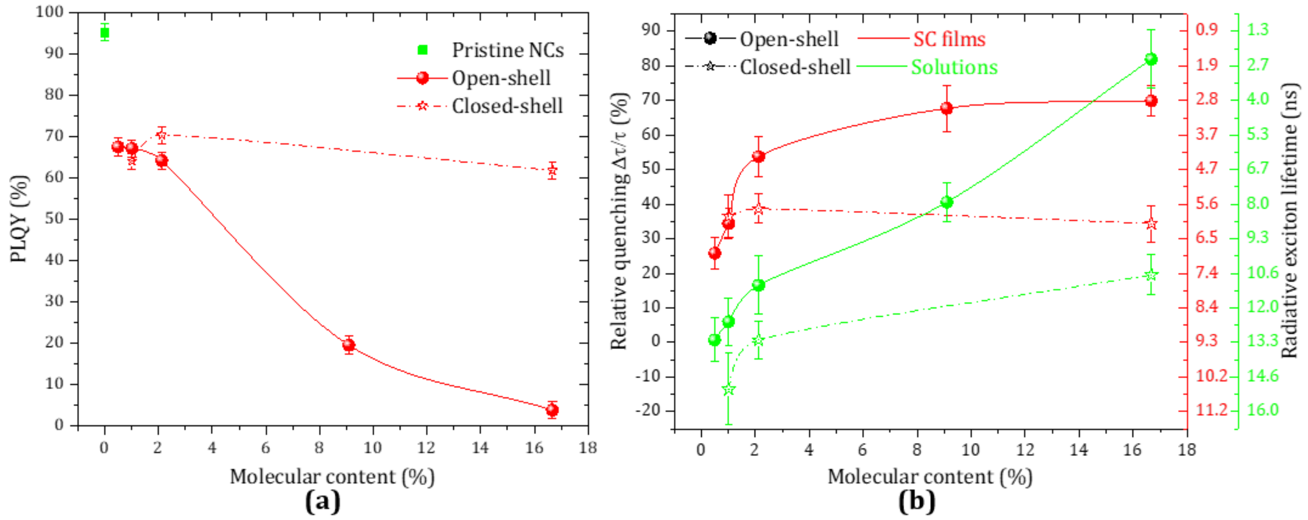

Fig. 4.12 Comparison of **(a)** the photoluminescence quantum yield queching (SC films) and **(b)** the relative radiative exciton lifetime quenching, in the Blatter-radical (open-shell) and Quinonimine (closed-shell) blend samples.

4% and exciton lifetime shortening up to ~70% for films. Notably, these quenching effects are quite more pronounced in films compared to solutions, apart from the highest radical content blend of 5:1, where though mixing in both the liquid and solid state may not be optimum as also hinted by the inhomogenous morphology obtained in the fluorescence microscopy of Fig. 4.5. For the main range of relative NC-radical ratios, the stronger quenching of the NC emission in the solid state, strongly suggests proximity-enabled interactions which are significantly more effective in the static, closed-packed environment provided by the film medium, facilitating closer and sustained interactions between nanocrystals and radicals.

In contrast, the closed-shell heterojunctions formed with Quinonimine molecules demonstrate a substantially smaller impact on the NC luminescence. The PLQY remains high (around 60-63%) even at higher molecular contents in the heterojunctions, displaying a small overall reduction compared to the NC pristine samples. Quenching of the exciton dynamics is somewhat larger compared to the PL QY quenching in thin films but importantly appears independent of the relative content of NC:organic.

These experimental observations can be rationalized effectively by examining the frontier orbital energy alignment of the two molecular systems with respect to the nanocrystal band edges. For the open-shell Blatter radical heterojunction, as suggested by the DFT calculations in Fig. 4.4, the alignment of the radical's SOMO at -4.23 eV situates it energetically between the conduction band minimum (CBM) at -3.44 eV and valence band maximum (VBM) at -5.83 eV of the $CsPbBr_3$ NCs, as shown in Fig. 4.13. This configuration enables thermodynamically favorable bidirectional charge transfer pathways, electron transfer from the nanocrystal CBM to the radical SOMO, and or hole transfer from the nanocrystal VBM, forming a non-emissive charge-separated state that effectively quenches the PL[6] and shortens the exciton lifetime.

---

[6] Referring to how excitons dissociate non-radiatively when charge transfer occurs in the heterojunction.

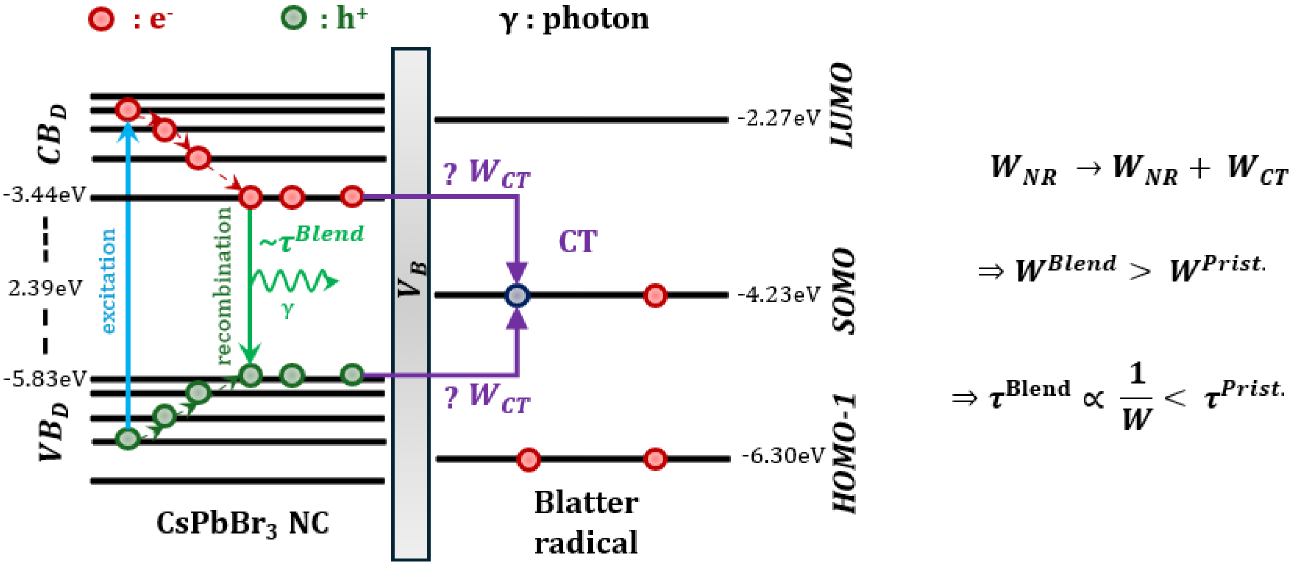

Fig. 4.13 Jablonski diagram of the proposed interaction, at the interface of the $CsPbBr_3$ NC - Blatter radical/Open-shell blend samples.

In contrast, the closed-shell, Quinonimine heterojunction shows a mismatched orbital alignment, with its LUMO at -3.31 eV closely aligned or slightly above the nanocrystal CBM, and its HOMO at -5.56 eV situated above the nanocrystal VBM.

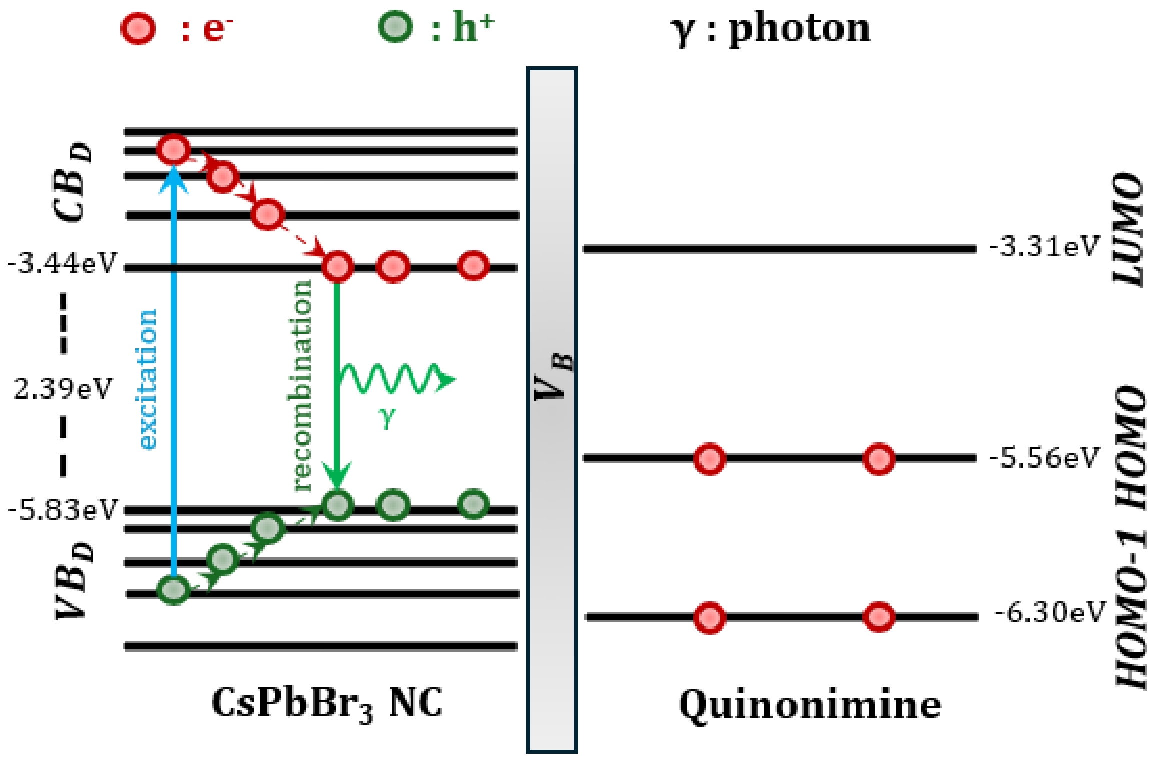

Fig. 4.14 Jablonski diagram of the proposed interaction, at the interface of the $CsPbBr_3$ NC - Quinonimine/Closed-shell blend samples.

In general, the following main phenomena can compete against the nanocrystal (NC) radiative process within the hybrid heterojunctions:

1. **Charge Transfer (CT):** Transfer of electrons or holes from the NCs, where NCs act as electron/hole donors.
2. **Energy Transfer (ET):** Transfer of excitonic energy from the NCs to the organic molecules, where NCs act as energy donors.
3. **Surface Defect Formation:** Formation of trap states at the organic/NC heterointerface, which can facilitate non-radiative recombination.
4. **Dielectric Screening & Local Environment Effects:** Modifications of exciton binding energy and recombination rates due to changes in the dielectric constant or environment.
5. **Chemical Interactions:** Photoinduced or spontaneous chemical reactions at the NC-organic interface, which may passivate or disrupt emissive states.

To rationalize against the other 4 possible processes, it is useful to examine the frontier orbital energy alignment of the two molecular systems with respect to the NC band edges shown in Fig. 4.13 and 4.14.

For the open-shell Blatter radical heterojunction, as suggested by the DFT calculations in Fig. 4.4, the alignment of the radical's SOMO at -4.23 eV places it energetically between the conduction band minimum (CBM) at -3.44 eV and valence band maximum (VBM) at -5.83 eV of the $CsPbBr_3$ NCs, as shown in Fig. 4.13. This configuration enables thermodynamically photoinduced charge transfer pathways that include both electron transfer from the nanocrystal CBM to the radical SOMO, and hole transfer from the nanocrystal VBM. In such case, the NC exciton dissociates, quenching the NC emission and shortening the PL exciton lifetime.

Energy (or exciton) transfer from the NCs to the SOMO-LUMO (~ 2 eV) and to the HOMO-1–SOMO (~ 2.1 eV) of the radical are energetically allowed but are less probable than charge transfer. For dipole-dipole (Förster) type of transfer, a high overlap of the donor emission (NC) with the acceptor absorption (Radical) is required, which does not exist in our blends based on the respective optical data (Fig. 4.5 and 4.6). On the other hand, Dexter transfer may be more relevant to the unpaired electron of the radical SOMO level. However, there is no additional spectroscopic signature such as a visible radical emission in the blends that would indicate some energy funneling from the NCs. Dexter transfer is a short-range process, as it requires significant overlap between the wavefunctions of the nanocrystals and radicals, as discussed in section 1.1.3.4, which is unlikely without direct bonding, such as when radicals displace native ligands (e.g., OA, OAm, or DDAB) and bind directly to the NC surface. Such a ligand exchange process cannot be excluded and it will be probed in next actions via surface sensitive techniques such as Fourier transform infrared (FTIR) and solid state nuclear magnetic resonance (NMR) spectroscopy. However, we argue that upon such surface chemistry modification, the spectral changes in the NC absorption and emission relative to the pristine NCs would be noticeable, which is not the case here.

Further insight may be gained by investigating the ultrafast processes occurring at the NC-organic heterointerface through transient absorption (TA) pump probe spectroscopy. Preliminaty measurements[7]The pump probe 400 nm excitation source primarily photoexcites the CsPbBr$_3$ nanocrystal component, as direct absorption by the Blatter radicals is minimal at this wavelength[8] . Figure 4.15a presents the normalized differential transmission (ΔT/T) spectra, revealing a pronounced ground-state bleach (GSB) at approximately ∼496 nm associated with the NC excitonic transition. Additionally, a subtle yet notable absorption feature appears around ∼475 nm in both blends based on the closed and open shell molecules associated with transitions in the organic part of the blends.

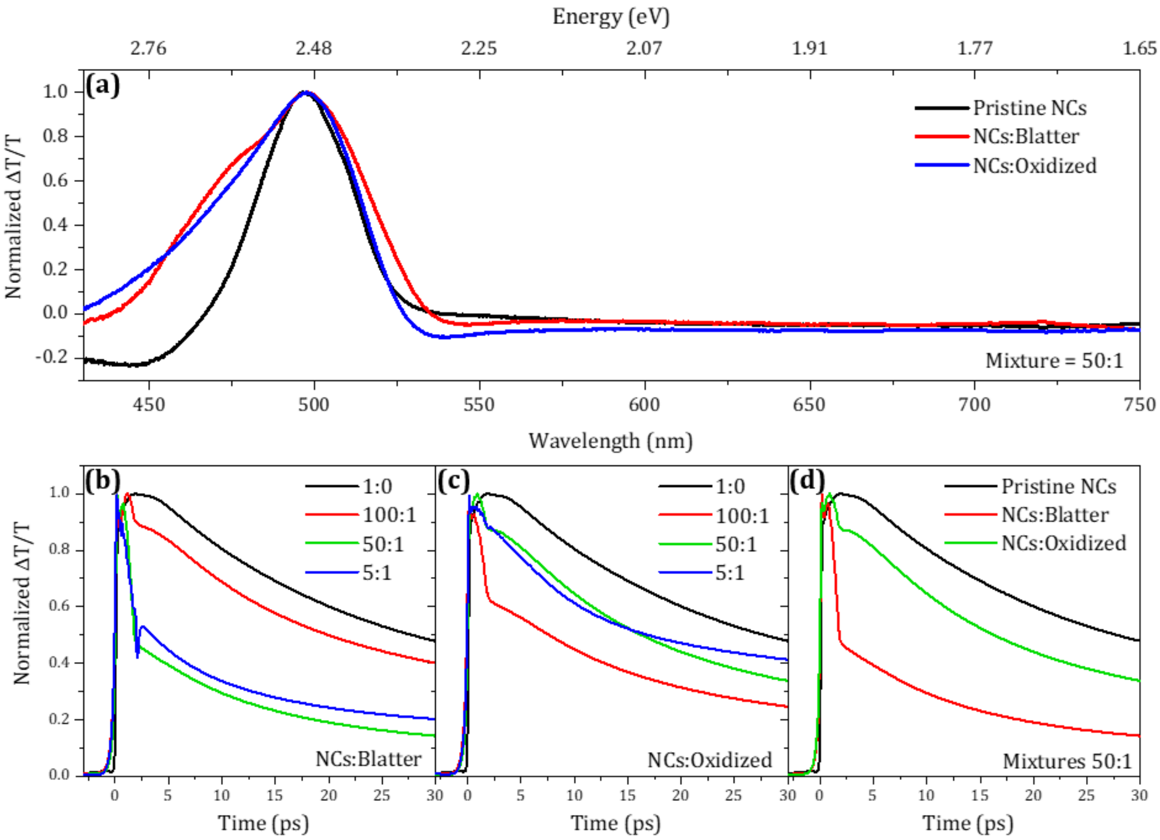

Fig. 4.15 Transient absorption spectrocopy decay measurements of **(b)** the nanocrystal-blatter radical blend and **(c)** the nanocrystal-quinonimine blend samples. The decays were derived by integrating an area of ±10nm around the peak of the pristine sample's ground state bleaching wavelength, as shown in **(a)**, with a delay of approximately 1.5ps between pump and probe. A comparative plot **(d)** of the decays of the 50:1 volume ratio blends, shows significantly enhanced early-time effects in the blatter radical blends.

Our preliminary analysis focuses on the dynamics of Figures 4.15b,c. Integration over ∼ ±10nm around the ground state bleaching peak clearly indicates accelerated early-time decay in blends containing Blatter radicals compared to pristine NCs, strongly indicative of ultrafast

---

[7] These were taken days before the submission date of this thesis to give a qualitative picture of the carrier dynamics of our samples. More data will be required for a conclusive picture.

[8] A meaningful reference measurement for Blatter radicals alone was not achievable due to their negligible absorption at 400nm.

electron or hole transfer transitions. This charge extraction scales as expected with radical concentration[9] , exhibiting consistently accelerated dynamics in contrast to blends with Quinonimine where no consistent trend with the organic molecule content is observed. The comparative analysis in Figure 4.15d underscores the more significant charge-transfer effect in Blatter radical blends.

Collectively, the transient absorption measurements align well with the conclusions drawn from time-resolved photoluminescence (TRPL). The reduction in exciton lifetime and significant photoluminescence quenching strongly support an ultrafast electron-transfer scenario, while the systematic blue shift in emission across varied radical concentrations emphasizes the role of dielectric modifications around the NCs. Ultimately, our observations underscore that the interplay between ultrafast charge-transfer processes and dielectric screening effects is central to the complex photophysics observed at hybrid organic-inorganic interfaces.

In the end, we are left with two processes that are most likely at play simultaneously: charge transfer and dielectric screening effects. The presence of significant photoluminescence quenching and decreased exciton lifetimes strongly supports a scenario in which charge transfer from the CsPbBr3 nanocrystals to the Blatter radicals occurs, given the low likelihood of other carrier transfer processes such as FRET and DET. Moreover, the observed blue shift in the emission spectra of the nanocrystals across different radical concentrations points convincingly toward dielectric modifications in the local nanocrystal environment induced by the presence of Blatter radicals. Together, these mechanisms likely coexist, intricately shaping the photophysical behavior observed at this interface, and suggesting that a comprehensive understanding of exciton dynamics at hybrid organic-inorganic interfaces must account for both electronic and dielectric interactions.

---

[9] With the seemingly minute inconsistency between the 50:1 and 5:1 volume ratios possibly explained by film-to-film errors or saturation effects.

Conclusions

This thesis has explored the photophysical behavior of hybrid heterojunctions formed between $CsPbBr_3$ perovskite nanocrystals (NCs) and Blatter radicals, motivated by the potential applications of these hybrid systems in optoelectronics and spintronics. Employing steady-state and time-resolved photoluminescence spectroscopy, the thesis provides clear experimental evidence for significant interactions between the NCs and Blatter radicals.

Firstly, a pronounced photoluminescence (PL) quenching effect was observed upon incorporating Blatter radicals, accompanied by a substantial shortening of exciton lifetimes. This strongly suggests the occurrence of efficient charge transfer (CT) processes, confirming that Blatter radicals effectively act as electron acceptors, drawing carriers from the perovskite NCs. This conclusion is further reinforced by the comparative investigation of open-shell radicals and their closed-shell Quinonimine counterparts, which helped establish that energy transfer mechanisms, specifically Förster Resonance Energy Transfer (FRET), play only a minor role, if any, under the studied conditions.

Secondly, the systematic blue-shift in NC emission with increasing radical concentration highlighted the significant impact of dielectric screening effects. This trend points toward modifications in the local dielectric environment surrounding the perovskite NCs caused by the organic radicals. Such dielectric effects not only alter the NC exciton energy landscape but also indicate that the interface chemistry and molecular environment critically influence exciton recombination pathways.

Ultimately, the findings highlight that the photophysical processes in $CsPbBr_3$-Blatter radical heterojunctions are more than likely governed predominantly by concurrent charge transfer and dielectric environment alterations. Future work could involve further application of transient absorption spectroscopy to gain deeper insights into carrier dynamics within the nanocrystal-radical heterojunctions. This technique would allow for time-resolved tracking of excited state processes and charge transfer mechanisms. Additionally, FTIR and NMR spectroscopy could be employed to better understand the chemical interactions and bonding characteristics between the $CsPbBr_3$ nanocrystals and the Blatter radicals, providing complementary structural and compositional information to support the optoelectronic findings.

Bibliography

[1] Quinten A. Akkerman, Gabriele Rainò, Maksym V. Kovalenko, and Liberato Manna. Genesis, challenges and opportunities for colloidal lead halide perovskite nanocrystals. *Nature Materials*, 17(5):394–405, 2018.

[2] N.W. Ashcroft and N.D. Mermin. *Solid State Physics.* Saunders College Publishing, Fort Worth, 1976.

[3] Peter Atkins and Ronald Friedman. *Molecular Quantum Mechanics.* Oxford University Press, Oxford, United Kingdom, 4th edition, 2005.

[4] Jeffrey E. Baldwin, Matthew D. Krzyaniak, and Michael R. Wasielewski. Stable organic radicals: Fundamentals and applications. *Chemical Reviews*, 120(2):500–599, 2020.

[5] Anne C. Berends, Freddy T. Rabouw, Frank C. M. Spoor, Eva Bladt, Ferdinand C. Grozema, Arjan J. Houtepen, Laurens D. A. Siebbeles, and Celso de Mello Donegá. Radiative and nonradiative recombination in cuins2 nanocrystals and cuins2-based core/shell nanocrystals. *The Journal of Physical Chemistry Letters*, 7(17):3503–3509, 2016. PMID: 27552674.

[6] Andrey A. Berezin, Georgia Zissimou, Christos P. Constantinides, Yassine Beldjoudi, Jeremy M. Rawson, and Panayiotis A. Koutentis. Route to benzo- and pyrido-fused 1,2,4-triazinyl radicals via n'-(het)aryl-n'-[2-nitro(het)aryl]hydrazides. *The Journal of Organic Chemistry*, 79(1):314–327, 2014. PMID: 24350615.

[7] Stephen M. Cohen. The fluorolog®-3 modular spectrofluorometer, n.d. Accessed: 2025-05-08.

[8] Alexander L. Efros and Louis E. Brus. Nanocrystal quantum dots: From discovery to modern development. *ACS Nano*, 15(4):6192–6210, 2021. PMID: 33830732.

[9] Nadesh Fiuza-Maneiro, Kun Sun, Iago López-Fernández, Sergio Gómez-Graña, Peter Müller-Buschbaum, and Lakshminarayana Polavarapu. Ligand chemistry of inorganic lead halide perovskite nanocrystals. *ACS Energy Letters*, 8(2):1152–1191, 2023.

[10] M. Fox. *Optical Properties of Solids.* Oxford Master Series in Physics. OUP Oxford, 2010.

[11] David J. Griffiths and Darrell F. Schroeter. *Introduction to quantum mechanics.* Cambridge University Press, Cambridge ; New York, NY, third edition edition, 2018.

[12] Georgina Karecla, Paris Papagiorgis, Nasia Panagi, Georgia A. Zissimou, Christos P. Constantinides, Panayiotis A. Koutentis, Grigorios Itskos, and Sophia C. Hayes. Emission from the stable blatter radical. *New Journal of Chemistry*, 41(16):8604–8613, 2017.

[13] Hamamatsu Photonics K.K. Laser-driven light source ldls – eq series, 2022. Accessed: 2025-05-08.

[14] Victor I. Klimov. *Nanocrystal Quantum Dots.* CRC Press, 2nd edition, 2010.

[15] Yongfeng Liu, Shi Tang, Junpeng Fan, Eduardo Gracia-Espino, Jinpeng Yang, Xianjie Liu, Satoshi Kera, Mats Fahlman, Christian Larsen, Thomas Wågberg, Ludvig Edman, and Jia Wang. Highly soluble cspbbr3 perovskite quantum dots for solution-processed light-emission devices. *ACS Applied Nano Materials*, 4(2):1162–1174, 2021.

[16] Konstantinos Manolopoulos, Martin Tschurl, and Stefan Kupfer. Stable blatter-type radicals for molecular electronics. *New Journal of Chemistry*, 45(12):5537–5546, 2021.

[17] Ossila. Quartz cuvettes, n.d. Accessed: 2025-05-08.

[18] Ossila. Spin coater, n.d. Accessed: 2025-05-08.

[19] Paris Papagiorgis, Marios Sergides, Andreas Manoli, Modestos Athanasiou, Caterina Bernasconi, Fedros Galatopoulos, Apostolos Ioakeimidis, Constantinos Nicolaides, Epameinondas Leontidis, Theodossis Trypiniotis, Stelios Choulis, Maryna I. Bodnarchuk, Maksym V. Kovalenko, Andreas Othonos, and Grigorios Itskos. The impact of ligand removal on the optoelectronic properties of inorganic and hybrid lead halide perovskite nanocrystal films. *Advanced Optical Materials*, 12(3):2301501, 2024.

[20] Paris G. Papagiorgis. *Spectroscopic Studies of Nanocrystal Solids Functionalized for Optoelectronic Applications.* Ph.d. dissertation, University of Cyprus, Nicosia, Cyprus, 2018.

[21] PerkinElmer. Lambda 1050+ uv/vis/nir spectrophotometer, n.d. Accessed: 2025-05-08.

[22] Freddy Rabouw and Celso Donega. Excited-state dynamics in colloidal semiconductor nanocrystals. *Topics in Current Chemistry*, 374, 08 2016.

[23] Sanghyun Rhee, Kyungwon An, and Kyung-Tae Kang. Recent advances and challenges in halide perovskite crystals in optoelectronic devices from solar cells to other applications. *Crystals*, 11(1):39, 2021.

[24] Shuxia Tao, Isabelle Schmidt, Geert Brocks, Jin Jiang, Ionut Tranca, Klaus Meerholz, and Selina Olthof. Absolute energy level positions in tin- and lead-based halide perovskites. *Nature Communications*, 10(1):2560, 2019.

[25] Stefan Wehr, Tobias Fuchs, and Martin Wenderoth. The puzzle of negative magnetoresistance in blatter radical molecular junctions solved. *Journal of Physical Chemistry Letters*, 16(3):865–871, 2025. Preprint, accessed 2025-05-22.

[26] Negin Yazdani, Simon Andermatt, Maksym Yarema, et al. Charge transport in semiconductors assembled from nanocrystal quantum dots. *Nature Communications*, 11:2852, 2020.